Full- and Reduced-Order State-Space Modeling of Wind Turbine Systems with Permanent Magnet Synchronous Generator

Christoph M. Hackl [1,*,†] , **Pol Jané-Soneira** [2,†] , **Martin Pfeifer** [2,†] , **Korbinian Schechner** [3,*,†] **and Sören Hohmann** [2]

1   Department of Electrical Engineering and Information Technology, Munich University of Applied Sciences, Lothstraße 64, 80335 München, Germany
2   Institute of Control Systems (IRS), Karlsruhe Institute of Technology (KIT), Kaiserstraße 12, 76131 Karlsruhe, Germany; pol.soneira@student.kit.edu (P.J.-S.); martin.pfeifer@kit.edu (M.P.); soeren.hohmann@kit.edu (S.H.)
3   Research Group "Control of Renewable Energy Systems", Munich School of Engineering, Technical University of Munich, Lichtenbergstraße 4a, 85748 Garching, Germany
*   Correspondence: christoph.hackl@hm.edu (C.M.H.); korbinian.schechner@tum.de (K.S.); Tel.: +49-89-1265-3417 (C.M.H.); +49-89-289-52720 (K.S.)
†   These authors contributed equally to this work.

Abstract: Full-order state-space models represent the starting point for the development of advanced control methods for wind turbine systems (WTSs). Regarding existing control-oriented WTS models, two research gaps must be noted: (i) There exists *no* full-order WTS model in form of *one* overall ordinary differential equation that considers all dynamical effects which significantly influence the electrical power output; (ii) all existing reduced-order WTS models are subject to rather arbitrary simplifications and are *not* validated against a full-order model. Therefore, in this paper, two full-order nonlinear state-space models (of 11th and 9th-order in the (a, b, c)- and (d, q)-reference frame, resp.) for variable-speed variable-pitch permanent magnet synchronous generator WTSs are derived. The full-order models cover all relevant dynamical effects with significant impact on the system's power output, including the switching behavior of the power electronic devices. Based on the full-order models, by a step-by-step model reduction procedure, two reduced-order WTS models are deduced: A non-switching (averaging) 7th-order WTS model and a non-switching 3rd-order WTS model. Comparative simulation results reveal that all models capture the dominant system dynamics properly. The full-order models allow for a detailed analysis covering the high frequency oscillations in the instantaneous power output due to the switching in the power converters. The reduced-order models provide a time-averaged instantaneous power output (which still correctly reflects the energy produced by the WTS) and come with a drastically reduced complexity making those models appropriate for large-scale power grid controller design.

Keywords: wind turbine system; wind energy conversion system; dynamic modeling; control design model; control system; operation management; switching behavior; nonlinear dynamics; model reduction; comparative simulation

1. Introduction

Sustainable electrical energy is a major concern of modern society. Wind power represents a renewable and carbon-free energy resource which can be made available on a large scale by wind turbine systems (WTSs). During the last two decades, electricity generation by wind power experienced

a vast expansion leading to a global cumulative installed generation capacity of about 539.6 GW in 2017 [1]. A WTS is a complex system, which covers multiple physical domains, as aerodynamical, mechanical and electrical subsystems. Due to this complexity, studies which have to incorporate the behavior of WTSs mostly apply model-based methods, where the starting point is the derivation of a suitable WTS model.

The history of WTS modeling goes back to the end of the 1970s, where first wind power impact studies were undertaken [2]. In the 1980s, first WTS models for fixed-speed WTSs were presented [3] and applied to large scale transient stability computer programs [4]. Since that time, there have been numerous models for induction generator (IG) WTSs [5–9], doubly fed induction generator (DFIG) WTSs [10–18] and permanent magnet synchronous generator (PMSG) WTSs [4,7,8,17,19–26]. The above-mentioned models are developed for an application in numerical simulations and mainly focus on the electrical subsystems (For wind turbine system models considering more sophisticated blade designs, aerodynamics, mechanical loading or tower vibrations, please see, e.g., [27] or [28]). In general, these models consist of a number of differential and algebraic equations with no specification of control inputs, system states, and control outputs.

Control-oriented models represent an indispensable basis for the development of advanced (state-space) control methods for WTSs [29–38]. In contrast to the above-mentioned simulation models, control-oriented models require a specification of control inputs, system states and control outputs. Moreover, a representation of the model as system of explicit differential equations is crucial. Major goal is to obtain *one* overall (vector-valued) ordinary differential equation describing the *whole* system. Thus, the available WTSs simulation models can in general not be used for the development of state-space control methods or an overall stability analysis. Due to the high system complexity and significant nonlinearities in WTSs, the conversion from a WTS simulation model to a WTS state-space model is a challenging task.

The most notable representation of control-oriented models is the state-space representation. In literature, there has been a significant number of publications addressing the derivation of full-order state-space models for WTSs. In ref. [39], a ninth-order linear state space model of a PMSG wind turbine is derived. The model considers the mechanical subsystem, the PMSG, and the electrical power converter. However, essential system dynamics and intrinsic nonlinearities, e.g., pitch angle or nonlinear machine dynamics and switching in the power electronics, are neglected. The authors of ref. [29] present a seventh-order nonlinear state-space model for IG variable-speed WTSs. Again, pitch system dynamics and switching behavior of the power converters are not considered. In ref. [40], a 16th-order nonlinear state-space model for a PMSG WTS is developed. The model describes the closed-loop WTS and thus combines the modeling of the physics and control schemes. Eight of 16 state variables are intermediate variables which are used to model the machine-side and grid-side power converter controllers. Nevertheless, crucial dynamics of the physical system, such as the DC link dynamics (interlinking energy buffer between machine and grid side), are not considered in this model. In ref. [41], a differential-algebraic state-space model of DFIG WTSs is presented. The model is not formulated as system of explicit differential equations which hampers its application to control design. In ref. [42], non-switching discrete-time models for DFIG and PMSG WTSs for real-time power-hardware-in-the-loop emulations are presented. The subsystem models of electrical subsystems are formulated in state-space representation. However, there is no model for the overall WTS. In ref. [38], the authors present a model for PMSG wind turbines, which incorporates generator dynamics, power converter dynamics (including switching) and grid dynamics. However, turbine dynamics and pitch system dynamics are not considered. Generator and grid side are modeled in state-space form, but the authors do not provide an overall full-order state space model of the whole WTS.

Besides full-order models, there have been various publications addressing reduced-order models of WTSs. Reduced-order models also describe the behavior of an entire WTS, e.g., in terms of power output. However, one or more subsystems of the WTS are simplified or even neglected which leads,

compared to full-order WTS models, to a reduced order of the model which might not be capable of reduplicating the dominant and crucial dynamics of the original system. In ref. [30], a state-space model of variable-speed variable-pitch DFIG WTSs is proposed and used for model predictive control design. The electrical part is modeled as a first-order system which represents a significant (over-)simplification. In ref. [32], a fifth-order linear state-space model for variable-speed variable-pitch WTSs is presented. The model describes the closed-loop WTS. Thus, some states do not represent physical states but controller states describing, e.g., a PI controller. This model completely neglects the electrical components of the WTS. In ref. [35], continuous-time and discrete-time state-space models of the electrical power conversion system of a PMSG WTS are developed but the mechanical part of the WTS is not covered. In ref. [31], a linear state-space model of WTSs is presented. The linear model describes the mechanics of the system including pitch angle dynamics. However, the electrical part of the WTS is neglected and the intrinsic nonlinearities in WTSs are not included. In ref. [43], a linear state-space model for WTSs with focus on aerodynamics and mechanics is presented. In ref. [33], a simplified nonlinear third-order state-space model only for the mechanics of a WTS is presented. In ref. [34], a fifth-order nonlinear state-space model for the DFIG of a WTS is presented. However, the power converter, the pitch system dynamics and the mechanical part of the system are not considered. In ref. [36], a second-order linear state-space model for the drive system of PMSG WTSs is developed neglecting the nonlinear behavior of real WTS.

Regarding the literature review above on control-oriented modeling of WTSs, two research gaps must be noted: (i) There exists no full-order model (in form of *one* overall ordinary differential equation) that considers all dynamical effects which significantly influence the WTS's power output and (ii) all existing reduced-order WTS models are subject to rather arbitrary simplifications of one or more subsystems. To the best of the authors' knowledge, there does *not* exist a publication that specifically (a) addresses a detailed WTS full-order state-space model derivation; (b) provides a structured and physically motivated model order reduction technique based on the derived full-order model; (c) discusses the effects of the simplifications on the validity of the reduced-order models and (d) validates the reduced-order models against the derived and underlying full-order model.

This publication tries to fill the research gaps (i) and (ii) stated above by introducing state-space models for the dynamic relation between the input wind speed and produced electrical output in variable-speed variable-pitch PMSG WTSs. The paper comes with five main contributions: (a) The derivation of two full-order state-space models for variable-speed PMSG WTSs, which apture all dynamical effects (including the switching behavior) that significantly affect the power output of the system. For sake of comprehensibility and consistency, the models are developed step by step by recapitulating the basic physical relations of variable-speed variable-pitch PMSG WTSs; (b) The structured derivation of two reduced-order models for variable-speed variable-pitch PMSG WTSs based on a stepwise and physically motivated model reduction of the proposed full-order models from (a); (c) the motivating (simplifying) assumptions for the presented model reduction are discussed and (d) the derived full-order and reduced-order models are compared by numerical simulations and the validity of the reduced-order models (in the sense of capturing the dominant system behavior) is shown and (e) advantages and drawbacks concerning model accuracy and computational complexity of each proposed model are discussed.

The remainder of this paper is organized as follows. In Section 2, the WTS under consideration is briefly described. In Section 3, a full-order state-space model of the physics of the WTS is derived which is then formulated in the three-phase (a, b, c)- and synchronously rotating (d, q)-reference frame. In order to simulate the closed-loop behavior of the WTS model, realistic control schemes are required. Thus, in Section 4, control and operation management systems are also presented. The control systems address wind speeds between cut-in and cut-out wind speed (regime II + III) and consider practical constraints such as saturation and integral windup. In Section 5, two reduced-order models are deduced from the proposed full-order model by a physically motivated model reduction method. In Section 6, the performance of the full-order model and the reduced-order models is compared

through numerical simulations. For the simulation of the closed-loop models, the control and operation management of Section 4 are applied. Finally, Section 7 provides a concluding overview and discussion of the presented models and results.

2. System Description

The considered system is shown in Figure 1 and represents a state of the art WTS: a variable-speed, variable-pitch, three bladed, horizontal axis, lift turbine in up-wind position. Only a single WTS is considered neglecting aerodynamical (e.g., wake effect) or electrical interactions between multiple turbines. Regarding the type of generator (in our case PMSG), the WTS might or might not comprise a gear between turbine and generator. The generator feeds the converted power through a full-scale back-to-back converter and grid-side filter to the point of common coupling (PCC). The transformer is not explicitly modelled, but could easily be added. The grid is assumed to be symmetrical and stiff, so that the grid-side voltage source inverter (VSI) operates in grid-feeding mode.
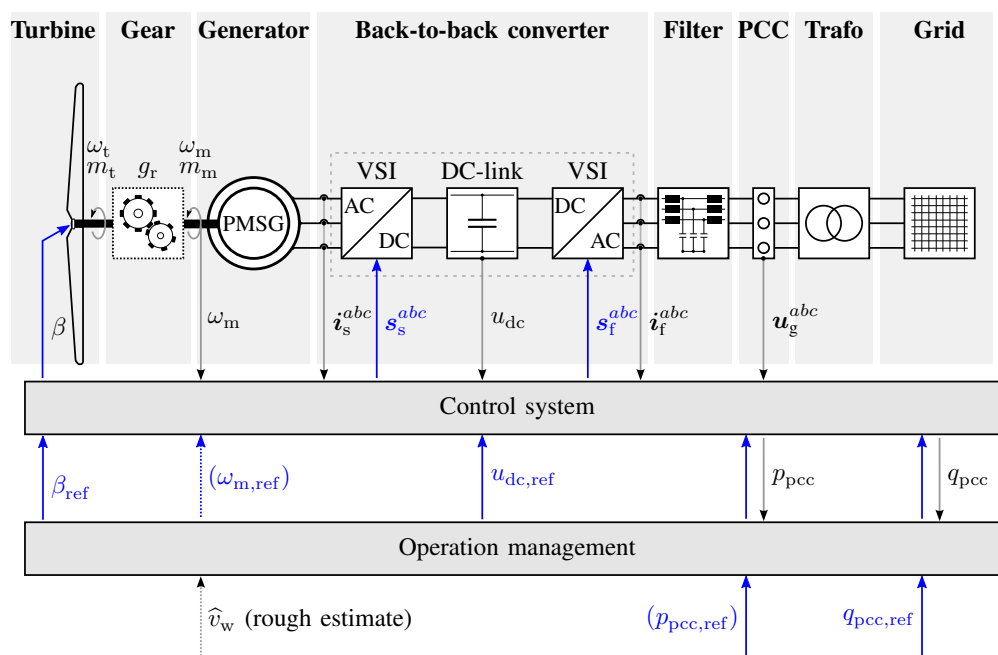

Figure 1. Overview of the core components of a WTS.

Depending on the actual wind speed v_w (in $\frac{m}{s}$), the WTS operates in one of the four regimes of operation. These four operation regimes are illustrated in Figure 2: For too less or too much wind (i.e., $v_w < v_{w,cut-in}$ in regime I and $v_w \geq v_{w,cut-out}$ in regime IV, resp.), the WTS is usually in idle mode or at standstill (Some companies use more sophisticated control methods for high winds, e.g. see patent [44] of REpower Systems for a reduced power production above $v_{w,cut-out}$ instead of a shut down.): The machine torque is zero, i.e., $m_m = 0\,\mathrm{N\,m}$, or the turbine angular velocity is zero, i.e., $\omega_t = 0\,\frac{rad}{s}$ and, hence, the turbine (output) power is also zero, i.e., $p_t = 0\,\mathrm{W}$, in regime I and IV. Since no power is fed into the grid, regimes I and IV will *not* be considered in this paper. In regime II, the wind speed is below the nominal wind speed $v_{w,rated}$ (in $\frac{m}{s}$) but at least the (minimum) cut-in wind speed $v_{w,cut-in}$ (in $\frac{m}{s}$). Due to the time-varying nature of the wind speed $v_w(\cdot)$, the turbine output power will vary between zero and nominal power $p_{t,rated}$ (in W), i.e., $0 \leq p_t < p_{t,rated}$. The goal is to extract as much wind power as possible, i.e., *maximum power point tracking* (MPPT) which is achieved by an underlying speed controller (see Section 4.1.2). In regime III, the wind speed is at least the nominal wind speed but lower than the (maximum) cut-out wind speed $v_{w,cut-out}$ (in $\frac{m}{s}$), i.e., $v_{w,rated} \leq v_w < v_{w,cut-out}$, and the torque m_m of the electrical machine is kept constant at its

nominal value (by constant feedforward torque control) and pitch control. The nominal output power is generated, i.e., $p_t = p_{t,rated}$ (see Section 4.1.3).
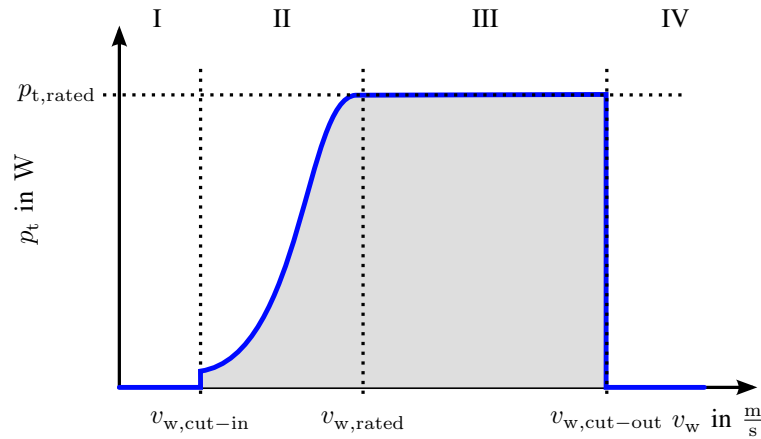

Figure 2. Operation regimes I to IV of a WTS.

In the following sections, the different hardware components illustrated in Figure 1 (such as turbine, gear, generator, back-to-back converter, filter, PCC) and physical quantities (e.g., ω_m, s_m^{abc}, u_{dc}) are described and introduced.

3. Full-Order Models

In this section, the detailed derivation of the complete physical model is presented. The modeling approach bases on the simulation model of [45]. It is extended by the pitch system dynamics, an explicit representation of the switching behavior and finally the overall reformulation as one state-space system model in the form of *one* vector-valued ordinary differential equation.

3.1. Aerodynamics, Turbine Torque and Drive Train

Aerodynamical conversion is achieved by the three rotor blades producing a turbine torque which accelerates the drive train and generator.

3.1.1. Aerodynamics

The turbine (rotor with three blades) converts part of the kinetic wind energy into rotational energy. The wind power $p_w(v_w) := \frac{1}{2} \varrho \pi r_t^2 v_w^3$ depends on air density ϱ (in $\frac{kg}{m^3}$), rotor radius r_t (in m), and wind speed v_w (in $\frac{m}{s}$). The extractable turbine power is limited by the Betz limit $c_{p,Betz} := 16/27 \approx 0.5926$ [46] and is given by

$$p_t(v_w, \omega_t, \beta) = c_p(v_w, \omega_t, \beta) \, p_w(v_w) \le c_{p,Betz} \, p_w(v_w). \tag{1}$$

The power coefficient $c_p(v_w, \omega_t, \beta) = c_p(\lambda, \beta)$ must be determined for each WTS and is a function of wind speed v_w, turbine angular velocity ω_t (in $\frac{rad}{s}$), and pitch angle β (in $°$) or of tip speed ratio $\lambda := \lambda(v_w, \omega_t) := \frac{r_t \omega_t}{v_w}$. Both, tip speed ratio λ (or ω_t) and pitch angle β, have a direct influence on the amount of power, the WTS can extract from the wind. Usually, the power coefficient $c_p(\lambda, \beta)$ is approximated by the following function $c_p : \mathcal{D} \to \mathbb{R}_{\ge 0}$ [47] (see Equation (2.38)),

$$c_p(\lambda, \beta) := c_1 \left[c_2 f(\lambda, \beta) - c_3 \beta - c_4 \beta^k - c_5 \right] e^{-c_6 f(\lambda, \beta)} \tag{2}$$

where $\mathcal{D} := \{ (\lambda, \beta) \in \mathbb{R}_{>0} \times \mathbb{R}_{\ge 0} \mid c_p(\lambda, \beta) \ge 0 \}$. The constants $c_1, \dots, c_6 > 0$, the exponent $k \ge 0$ and the continuously differentiable function $f : \mathcal{D} \to \mathbb{R}$ can be determined from measurements or by

aerodynamic simulations. Two exemplary power coefficient approximations for two different 2 MW WTSs are as follows [48] (Chaper 12):

- Power coefficient *without* pitch control system (i.e., $\beta = 0$) $c_{p,1}(\lambda, 0) := c_{p,1}(\lambda)$:

$$c_{p,1}(\lambda) := \left[46.4 \cdot \left(\frac{1}{\lambda} - 0.01 \right) - 2.0 \right] e^{-15.6 \left(\frac{1}{\lambda} - 0.01 \right)}, \tag{3}$$

  which has a global maximum at $\lambda^\star = 8.53$ with $c_{p,1}^\star := c_{p,1}(\lambda^\star) = 0.564$.

- Power coefficient *with* pitch control system (i.e., $\beta \geq 0$):

$$c_{p,2}(\lambda, \beta) := 0.73 \Bigg[151 \left(\frac{1}{\lambda - 0.02\beta} - \frac{0.003}{\beta^3 + 1} \right)$$
$$- 0.58\beta - 0.002\beta^{2.14} - 13.2 \Bigg] \cdot$$
$$\cdot \exp \left(-18.4 \left(\frac{1}{\lambda - 0.02\beta} - \frac{0.003}{\beta^3 + 1} \right) \right), \tag{4}$$

  which, for $\beta = \beta^\star = 0$, has its maximum at $\lambda^\star = 6.91$ with $c_{p,2}^\star := c_{p,2}(\lambda^\star, \beta^\star) = 0.441$.

The graphs of $c_{p,1}(\cdot)$ and $c_{p,2}(\cdot, \cdot)$ are shown in Figure 3. Both power coefficients are below the possible Betz limit of $c_{p,\text{Betz}} = 16/27 \approx 0.59$. The maximum value of $c_{p,1}(\cdot)$ is larger than that of $c_{p,2}(\cdot, \cdot)$. This does not hold in general but is a characteristic feature of the two WTSs considered in [49] (p. 9) and [50,51],
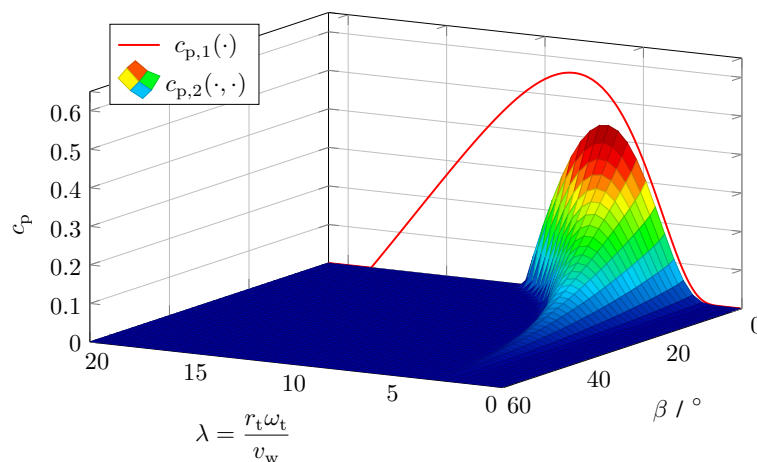
Figure 3. Graphs of the power coefficient approximations $c_{p,1}(\cdot)$ and $c_{p,2}(\cdot, \cdot)$ for a 2 MW WTS.

3.1.2. Pitch Control System

The pitch system allows to control the pitch angle β (in °) to its specified reference β_{ref} (in °). The nonlinear dynamics of the pitch control system are approximated by (A simplification of the pitch system dynamics given in [47] (Sections 2.3 and 5.5)).

$$\left. \begin{array}{rcl} \frac{\mathrm{d}}{\mathrm{d}t} \beta_\Diamond(t) & = & \mathrm{sat}_{-\dot{\beta}_{\max}}^{\dot{\beta}_{\max}} \left(\frac{1}{T_\beta} \left(-\beta(t) + \beta_{\text{ref}}(t) \right) \right), \\ \beta(t) & = & \mathrm{sat}_{0°}^{90°} \left(\beta_\Diamond(t) \right), \end{array} \right\} \tag{5}$$

with unsaturated pitch angle $\beta_\Diamond$ (in °) and initial value $\beta_\Diamond(0) = \beta_{\Diamond,0} \geq 0$ (in °), where $\dot{\beta}_{\max} > 0$ (in $\frac{°}{s}$) and T_β (in s) are the maximally feasible change rate of the pitch angle and (approximated) pitch control

system time constant, respectively (see Figure 4). The underlying current, speed and position control dynamics are neglected (for details see e.g., [48] (Section 11.2). The overall approximated dynamics show the dynamic behavior of a first-order lag system where output and change rate of the state are saturated, respectively.
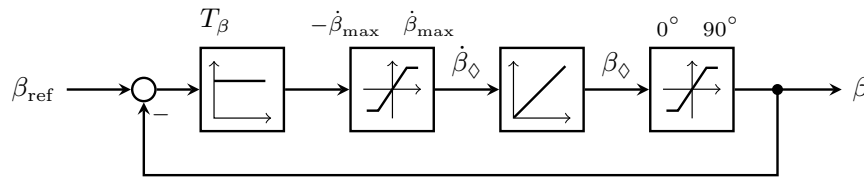

Figure 4. Block diagram of the approximated pitch system dynamics.

3.1.3. Turbine Torque

The turbine converts the kinetic energy of the wind into rotational energy. If friction losses are neglected then, from turbine power $p_t = m_t \omega_t$ with turbine torque m_t (in N m) and turbine angular velocity ω_t, the turbine torque can directly be computed as follows

$$m_t(v_w, \lambda, \beta) \overset{(1),(2)}{:=} \tfrac{1}{2} \varrho \, \pi \, r_t^3 \, v_w^2 \, \frac{c_p(\beta, \lambda)}{\lambda} = \tfrac{1}{2} \varrho \, \pi \, r_t^2 \, v_w^3 \, \frac{c_p(v_w, \omega_t, \beta)}{\omega_t} =: m_t(v_w, \omega_t, \beta). \tag{6}$$

The torque is a *nonlinear function* of pitch angle β, wind speed v_w and tip speed ratio λ or turbine angular velocity ω_t.

Remark 1. *The approximation (2) of the power coefficient $c_p(\cdot, \cdot)$ does* not *allow for the simulation of the start-up of a WTS, since $\lim_{\omega_t \to 0} m_t(v_w, \omega_t, \beta) = 0$ for all $v_w > 0$ and $\beta \geq 0$ [45]. The approximation (2) only yields physically meaningful results for $\lambda > 0$. At standstill, the accelerating torque would be zero.*

3.1.4. Drive Train

A gearbox transmits the mechanical turbine power via a shaft to the rotor of the generator. In modern WTSs, the turbine angular velocity ω_t is significantly lower than the angular velocity ω_m (in $\frac{rad}{s}$) of the machine (generator). Therefore, a step-up gearbox with ratio $g_r \gg 1$ is usually employed (exceptions are WTSs with "Direct Drive", i.e., $g_r = 1$, where the generator is connected directly to the turbine rotor). For a *rigid* coupling, generator (machine) and turbine angular velocities are related by $\omega_m = g_r \omega_t$. Hence, denoting the machine torque by m_m (in N m), turbine power p_t and turbine torque m_t are converted to the machine-side quantities as follows

$$p_m = \omega_m m_m = g_r \omega_t \frac{m_t}{g_r} = p_t. \tag{7}$$

Moreover, the inertias Θ_t and Θ_m (both in kg m^2) of turbine rotor (+hub) and machine rotor (+shaft) can be merged to the overall inertia $\Theta := \frac{\Theta_t}{g_r^2} + \Theta_m$ of the drive train. For simplicity, turbine-side and machine-side friction and elasticity in the shaft are neglected (for more details on friction modeling & compensation, and elastic drive train modeling, see [48] (Section 11.1.5 & Chaper 12) and [40,52]).

3.2. Electrical System in Three-Phase (a, b, c)-Reference Frame

In Figure 5, the (simplified) electrical network of a WTS with PMSG or IG is depicted. The machine-side network (left) shows the stator windings with stator phase voltages $\boldsymbol{u}_s^{abc} = (u_s^a, u_s^b, u_s^c)^\top$ (each in V), stator phase current $\boldsymbol{i}_s^{abc} = (i_s^a, i_s^b, i_s^c)^\top$ (each in A), stator phase resistance R_s (in Ω), and stator flux linkage $\boldsymbol{\psi}_s^{abc} = (\psi_s^a, \psi_s^b, \psi_s^c)^\top$ (each in Wb). The grid-side network (right) comprises filter and grid with filter phase voltages $\boldsymbol{u}_f^{abc} = (u_f^a, u_f^b, u_f^c)^\top$ (each in V), filter phase

currents $\boldsymbol{i}_f^{abc} = (i_f^a, i_f^b, i_f^c)^\top$ (each in A), filter resistance R_f (in Ω), filter inductance L_f (in H) and the grid phase voltages $\boldsymbol{u}_g^{abc} = (u_g^a, u_g^b, u_g^c)^\top$ (each in V). The (stepped-down) grid voltage $\boldsymbol{u}_g^{abc}$ is measured at the PCC. The transmission ratio of the transformer (not shown in Figure 5) is not explicitly modeled. Machine-side and grid-side converters exchange the stator power p_s (in W) and the filter power p_f (in W) via the DC-link. In the continuous operation of the WTS, the DC-link capacitance C_{dc} (in F) on average is *not* charged or discharged and no DC-link power, p_{dc} (in W), is exchanged within the circuit and the DC-link voltage u_{dc} remains (almost) constant. The (active) power p_{pcc} (in W) is fed into the grid at the PCC.
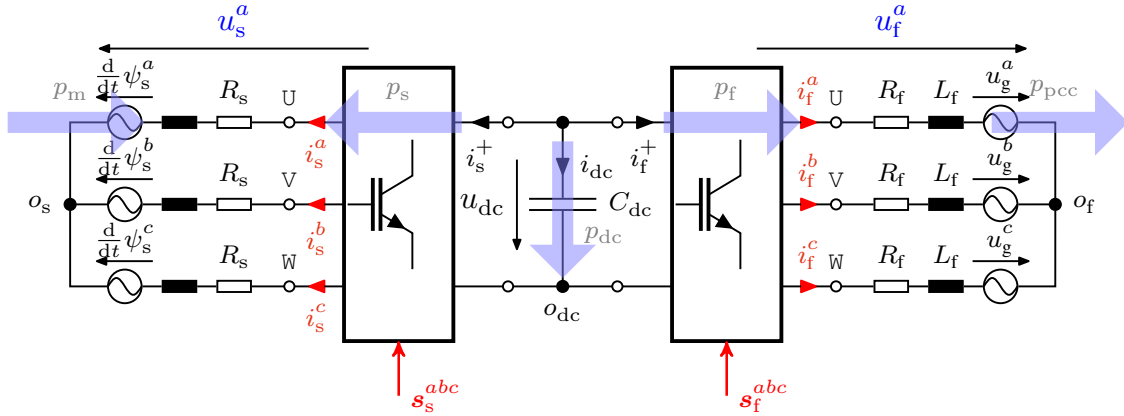

Figure 5. Electrical network of overall WTS: PMSG (**left**), back-to-back converter (**middle**) sharing a common DC-link, grid-side filter, point of common coupling (PCC) and balanced grid (**right**, neglecting the transformer).

3.2.1. Machine-sIde Dynamics (Electrical Machine/Generator and Drive Train)

For an isotropic PMSG, Kirchhoff's laws (see the electrical circuit in Figure 5) and Newton mechanics yield the following fifth-order dynamic system (for details see [48] (Chaper 14))

$$
\left.
\begin{aligned}
\frac{\mathrm{d}}{\mathrm{d}t}\boldsymbol{i}_s^{abc}(t) &= \left(\boldsymbol{L}_s^{abc}\right)^{-1}\left[\boldsymbol{u}_s^{abc}(t) - R_s\boldsymbol{i}_s^{abc}(t) + n_p\omega_m(t)\widehat{\psi}_{pm}\begin{pmatrix}\sin\left(n_p\phi_m(t)\right)\\ \sin\left(n_p\phi_m(t) - \frac{2}{3}\pi\right)\\ \sin\left(n_p\phi_m(t) - \frac{4}{3}\pi\right)\end{pmatrix}\right]\\
\frac{\mathrm{d}}{\mathrm{d}t}\omega_m(t) &= \frac{1}{\Theta}\Bigg[\frac{m_t\left(v_w(t),\omega_m(t)/g_r,\beta(t)\right)}{g_r} + \underbrace{n_p\boldsymbol{i}_s^{abc}(t)^\top\boldsymbol{J}_\Sigma\boldsymbol{\psi}_{pm}^{abc}(\phi_m(t))}_{=:m_m\left(\boldsymbol{i}_s^{abc}(t),\phi_m(t)\right)}\Bigg]\\
\frac{\mathrm{d}}{\mathrm{d}t}\phi_m(t) &= \omega_m(t)
\end{aligned}
\right\}
\tag{8}
$$

with initial values $\boldsymbol{i}_s^{abc}(0) = \boldsymbol{i}_{s,0}^{abc}$, $\omega_m(0) = \omega_{m,0}$ and $\phi_m(0) = \phi_{m,0}$, and where

$$
\boldsymbol{L}_s^{abc} := \begin{bmatrix} L_{s,m} + L_{s,\sigma} & -\frac{L_{s,m}}{2} & -\frac{L_{s,m}}{2} \\ -\frac{L_{s,m}}{2} & L_{s,m} + L_{s,\sigma} & -\frac{L_{s,m}}{2} \\ -\frac{L_{s,m}}{2} & -\frac{L_{s,m}}{2} & L_{s,m} + L_{s,\sigma} \end{bmatrix} \quad \text{and} \quad \boldsymbol{\psi}_{pm}^{abc}(\phi_m) := \widehat{\psi}_{pm}\begin{pmatrix}\cos\left(n_p\phi_m\right)\\ \cos\left(n_p\phi_m - \frac{2}{3}\pi\right)\\ \cos\left(n_p\phi_m - \frac{4}{3}\pi\right)\end{pmatrix} \tag{9}
$$

are inductance matrix $\boldsymbol{L}_{\mathrm{s}}^{abc} = (\boldsymbol{L}_{\mathrm{s}}^{abc})^{\top} > 0$ (with mutual inductance $L_{\mathrm{s,m}}$ and leakage inductance $L_{\mathrm{s},\sigma}$ such that $\boldsymbol{L}_{\mathrm{s}}^{abc} > 0$; both in H) and permanent magnet flux linkage vector $\boldsymbol{\psi}_{\mathrm{pm}}^{abc}$ (each in Wb), respectively; $\boldsymbol{J}_{\Sigma}$ is the rotation matrix as in (51). The dynamics in (8) incorporate electrical stator dynamics (the first three states) with stator flux linkage $\boldsymbol{\psi}_{\mathrm{s}}^{abc}(\boldsymbol{i}_{\mathrm{s}}^{abc}, \phi_{\mathrm{m}}) = \boldsymbol{L}_{\mathrm{s}}^{abc}\boldsymbol{i}_{\mathrm{s}}^{abc} + \boldsymbol{\psi}_{\mathrm{pm}}^{abc}(\phi_{\mathrm{m}})$ and the rotatory (mechanical) dynamics of the generator. The stator currents $\boldsymbol{i}_{\mathrm{s}}^{abc}$ and the mechanical angular velocity ω_{m} (and/or the mechanical angle ϕ_{m}) are measured and available for feedback control.

3.2.2. Power Electronics and DC-Link Dynamics (back-to-back Converter)

Although multi-level converters for the regulation of wind power plants are likely to be used in the future [53], the still widely used two-level back-to-back converter will be considered in this section. Each of the two voltage source converters (VSCs) of the back-to-back converter can be modeled as illustrated in Figure 6 by ideal switches (dynamics of the semi-conductors and free-wheeling diodes are neglected).
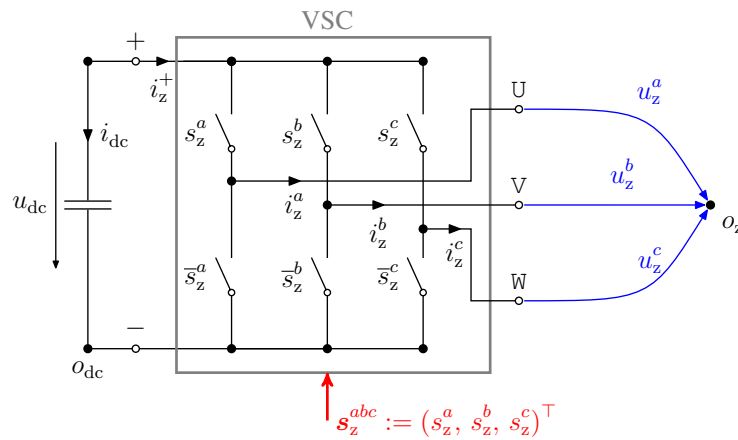

Figure 6. Electrical circuit of voltage source converter (VSC) with ideal switches and DC-link ($z \in \{s, f\}$).

The stator-side converter feeds the electrical machine (generator) with the phase voltages $\boldsymbol{u}_{\mathrm{s}}^{abc}$, while the filter-side converter applies the phase voltages $\boldsymbol{u}_{\mathrm{f}}^{abc}$ to the line filter. The output voltages of the converters depend on the DC-link voltage u_{dc} and are generated by adequate modulation, i.e. the application of an adequate sequence of the switching vectors $\boldsymbol{s}_{\mathrm{s}}^{abc} = (s_{\mathrm{s}}^a, s_{\mathrm{s}}^b, s_{\mathrm{s}}^c)^{\top}$ and $\boldsymbol{s}_{\mathrm{f}}^{abc} = (s_{\mathrm{f}}^a, s_{\mathrm{f}}^b, s_{\mathrm{f}}^c)^{\top}$. For the considered two-level VSCs, there exist eight possible switching vectors $(\boldsymbol{s}_{\mathrm{z}}^{abc})^{\top} \in \mathbb{S}_8 := \{000, 100, \ldots, 111\}$ for $z \in \{s, f\}$ (see Figure 6). Moreover, for balanced (i.e., $u_{\mathrm{s}}^a(t) + u_{\mathrm{s}}^b(t) + u_{\mathrm{s}}^c(t) = u_{\mathrm{f}}^a(t) + u_{\mathrm{f}}^b(t) + u_{\mathrm{f}}^c(t) = 0$ holds $\forall t \geq 0$.) voltages, the stator voltages and filter voltages are given by

$$\boldsymbol{u}_{\mathrm{z}}^{abc}(\boldsymbol{s}_{\mathrm{z}}^{abc}, u_{\mathrm{dc}}) = u_{\mathrm{dc}} \frac{1}{3} \underbrace{\begin{bmatrix} 2 & -1 & -1 \\ -1 & 2 & -1 \\ -1 & -1 & 2 \end{bmatrix}}_{=:\boldsymbol{T}_{\mathrm{vsc}}} \boldsymbol{s}_{\mathrm{z}}^{abc} \implies \|\boldsymbol{u}_{\mathrm{z}}^{abc}(\boldsymbol{s}_{\mathrm{z}}^{abc}, u_{\mathrm{dc}})\| \leq \widehat{u} := \frac{2}{3} u_{\mathrm{dc}} \tag{10}$$

for $z \in \{s, f\}$. Due to the limited DC-link voltage, each VSC can generate only a constrained phase voltage amplitude. The shared DC-link capacitor C_{dc} is charged or discharged via the DC-link

current $i_{\mathrm{dc}} = -i_{\mathrm{m}}^+ - i_{\mathrm{f}}^+$ (in A) which depends on the machine-side and grid-side currents, respectively (see Figure 5). The DC-link dynamics are given by

$$\frac{\mathrm{d}}{\mathrm{d}t} u_{\mathrm{dc}}(t) = \frac{1}{C_{\mathrm{dc}}} i_{\mathrm{dc}}(t) = \frac{1}{C_{\mathrm{dc}}} \left(-\underbrace{\boldsymbol{i}_{\mathrm{s}}^{abc}(t)^\top \boldsymbol{s}_{\mathrm{s}}^{abc}(t)}_{=:i_{\mathrm{s}}^+(t)} - \underbrace{\boldsymbol{i}_{\mathrm{f}}^{abc}(t)^\top \boldsymbol{s}_{\mathrm{f}}^{abc}(t)}_{=:i_{\mathrm{f}}^+(t)} \right), \tag{11}$$

with initial value $u_{\mathrm{dc}}(0) = u_{\mathrm{dc}}^0 > 0$ (in V).

The state-of-the-art modulation technique is the *space vector modulation* (SVM) which can reproduce *average phase voltage amplitudes* up to $\bar{u} := u_{\mathrm{dc}}/\sqrt{3}$. The classical *pulse width modulation* (PWM; without over-modulation) can reproduce average phase voltage amplitudes up to $\bar{u} := u_{\mathrm{dc}}/2$ (see [54] (pp. 658–720) and [55] (pp. 132–136)). Consider a feasible stator reference phase voltage vector $\boldsymbol{u}_{\mathrm{s,ref}}^{abc}(\cdot) \in \mathcal{C}(\mathbb{R}_{\geq 0}; [-\bar{u}, \bar{u}]^3)$ and a carrier signal $c_\wedge(\cdot) \in \mathcal{C}(\mathbb{R}_{\geq 0}; [-1, 1])$ (e.g., a sawtooth or triangular carrier signal with period $T_{\mathrm{sw}} = 1/f_{\mathrm{sw}}$ (in s) inversely proportional to the switching frequency f_{sw} (in Hz)). Then, PWM generates its pulse pattern by a simple and instantaneous comparison of normalized reference phase voltages and carrier signal. More precisely, the actual switching signal vector for PWM is obtained by

$$\boldsymbol{s}_{\mathrm{z}}^{abc}\left(\boldsymbol{u}_{\mathrm{z,ref}}^{abc}, u_{\mathrm{dc}}, t\right) := \begin{pmatrix} \sigma\left(\frac{u_{\mathrm{z,ref}}^a}{u_{\mathrm{dc}}/2} - c_\wedge(t)\right) \\ \sigma\left(\frac{u_{\mathrm{z,ref}}^b}{u_{\mathrm{dc}}/2} - c_\wedge(t)\right) \\ \sigma\left(\frac{u_{\mathrm{z,ref}}^c}{u_{\mathrm{dc}}/2} - c_\wedge(t)\right) \end{pmatrix} =: \sigma\left(\frac{\boldsymbol{u}_{\mathrm{z,ref}}^{abc}}{u_{\mathrm{dc}}/2} - \mathbf{1}_3 c_\wedge(t)\right) \in \mathbb{S}_8 \tag{12}$$

where $\sigma(\cdot)$ is the Heaviside (step) function. For SVM, the reference voltage vector $\boldsymbol{u}_{\mathrm{z,ref}}^{abc} = (u_{\mathrm{z,ref}}^a, u_{\mathrm{z,ref}}^b, u_{\mathrm{z,ref}}^c)^\top$ in (12) must be replaced [56] (pp. 267–271) by the expression

$$\boldsymbol{u}_{\mathrm{z,SVM,ref}}^{abc} = \left[\boldsymbol{u}_{\mathrm{z,ref}}^{abc} - \frac{\mathbf{max}(\boldsymbol{u}_{\mathrm{z,ref}}^{abc}) + \mathbf{min}(\boldsymbol{u}_{\mathrm{z,ref}}^{abc})}{2}\right] \tag{13}$$

where $\boldsymbol{u}_{\mathrm{z,ref}}^{abc}$ is the (original) reference vector from the control system and $\mathbf{max}(\boldsymbol{\xi}) := \max(\boldsymbol{\xi})\mathbf{1}_3$ and $\mathbf{min}(\boldsymbol{\xi}) := \min(\boldsymbol{\xi})\mathbf{1}_3$ return the minimal and maximal entries of the vector $\boldsymbol{\xi} \in \mathbb{R}^3$, respectively. The reference voltages are normalized with respect to $u_{\mathrm{dc}}/2$. For each phase $p \in \{a, b, c\}$ and $\mathrm{z} \in \{\mathrm{s}, \mathrm{f}\}$, the phase switching signal is high, i.e., $s_{\mathrm{z}}^p(t) = 1$, when the normalized reference phase voltage is larger than or equal to the carrier signal, i.e., $u_{\mathrm{z,ref}}^p(t) \geq c_\wedge(t)$; whereas the switching signal is low, i.e., $s_{\mathrm{z}}^p(t) = 0$, when the normalized reference is smaller than the carrier signal, i.e., $u_{\mathrm{z,ref}}^p(t) < c_\wedge(t)$.

Due to the finite (eight) number of switching vectors, not all reference voltage vectors can be generated instantaneously. The converter exhibits some delay which is inversely proportional to the switching frequency $f_{\mathrm{sw}} \gg 1\,\mathrm{Hz}$ [57] (pp. 525-526). On average, this delay can be quantified by the *inverter delay time* T_{avg} (in s) which is required to produce the *average output phase voltage vector* defined by [48] (Chapter 14)

$$\bar{\boldsymbol{u}}_{\mathrm{z}}^{abc}(t) := \frac{1}{T_{\mathrm{avg}}} \int_{t-T_{\mathrm{avg}}}^t \boldsymbol{u}_{\mathrm{z}}^{abc}(\tau)\,\mathrm{d}\tau \approx \boldsymbol{u}_{\mathrm{z,ref}}^{abc}(t - T_{\mathrm{avg}}) \tag{14}$$

for all $t \geq T_{\mathrm{avg}}$. The delay varies within the interval $T_{\mathrm{avg}} \in \left[\frac{1}{2f_{\mathrm{sw}}}, \frac{3}{2f_{\mathrm{sw}}}\right]$ [58] and depends on switching frequency f_{sw}, the selected modulation scheme (e.g., PWM or SVM) and its implementation (For most modern implementations, the reference voltages are sampled with the switching frequency f_{sw} at the maximum (or minimum) of the carrier signal $c_\wedge(\cdot)$ and held constant over the period $T_{\mathrm{sw}} = 1/f_{\mathrm{sw}}$, i.e., "*symmetrical sampling*" [48] (Chapter 14), [56] (Chapter 3.6).) (e.g., on FPGA, DSP or micro-processor).

3.2.3. Grid-Side Dynamics (Filter, PCC and Grid)

To induce sinusoidal phase currents to the power grid, a line filter must be used to filter out the switching behavior of the VSC. A simple *RL*-filter (in each phase) with filter inductance L_f (in H) and filter resistance R_f (in Ω) is considered. The grid-side converter generates the (filter) voltages u_f^{abc} which are applied to the filter and, due to the inductance L_f, lead to (approximately) sinusoidal filter phase currents i_f^{abc}. In the filter resistance R_f, the copper losses $R_f \|i_f^{abc}\|^2$ (in W) are dissipated and converted into heat. The grid-side electrical network with grid voltages u_g^{abc} is shown in Figure 5. According to Kirchoff's voltage law, the grid-side dynamics are given by

$$
\frac{\mathrm{d}}{\mathrm{d}t} i_f^{abc}(t) = \frac{1}{L_f} \left[u_f^{abc}(t) - R_f i_f^{abc}(t) - \hat{u}_g(t) \underbrace{\begin{pmatrix} \cos(\phi_g(t)) \\ \cos(\phi_g(t) - \frac{2\pi}{3}) \\ \cos(\phi_g(t) - \frac{4\pi}{3}) \end{pmatrix}}_{=:u_g^{abc}(t)} \right], \tag{15}
$$

with $i_f^{abc}(0) = i_{f,0}^{abc} \in \mathbb{R}^3$. The grid voltages $u_g^{abc}(\cdot)$ depend on a (possibly time-varying) amplitude $\hat{u}_g(\cdot) \geq 0\,\mathrm{V}$ and on a time-varying grid angle $\phi_g(\cdot) := \int_0^\cdot \omega_g(\tau)\,\mathrm{d}\tau + \phi_{g,0}$ (in rad). The angular grid frequency (In Europe, the grid frequency f_g (hence, $\omega_g = 2\pi f_g$) must remain within the frequency band $50\,\mathrm{Hz} \pm 0.5\,\mathrm{Hz}$ to ensure grid stability (see [59] (pp. 13, 20, 27).) ω_g (in $\frac{\mathrm{rad}}{\mathrm{s}}$) might also vary over time and the initial phase angle $\phi_{g,0}$ is usually unknown (a phase-locked loop is employed to detect $\phi_{g,0}$ and ω_g [45]). The grid voltages u_g^{abc} are measured before (or after) the transformer. The transformer steps up the voltage to a higher voltage level at the PCC (for example, to the medium voltage level of the power grid).

Remark 2. *In WTSs, also LCL-filters are used instead of RL-filters. The design of an LCL-filter allows for smaller inductances. Thus, an LCL-filter can be made smaller than an RL-filter. A detailed discussion of the LCL-filter design can be found in [60] (Chapter 11). The control of grid-side power converters connected to the grid via LCL-filters is discussed in e.g., [61,62].*

3.2.4. Power Output

The WTS outputs the active and reactive instantaneous powers p_{pcc} (in W) and q_{pcc} (in var) at the PCC which, for J_Σ as in (51) and $u_g^{abc}(t)$ as in (15), are respectively given by

$$
p_{pcc}(i_f^{abc}, t) = u_g^{abc}(t)^\top i_f^{abc} \qquad \text{and} \qquad q_{pcc}(i_f^{abc}, t) = u_g^{abc}(t)^\top J_\Sigma i_f^{abc}. \tag{16}
$$

3.2.5. Overall Dynamics in Nonlinear State-Space Representation

The overall model is of 11th order and considers switching. For state vector

$$
x := \Big(\underbrace{(x_1, x_2, x_3)}_{=:x_{1\text{-}3}^\top}, x_4, x_5, x_6, \underbrace{(x_7, x_8, x_9)}_{=:x_{7\text{-}9}^\top}, x_{10}, x_{11} \Big)^\top := \big((i_s^{abc})^\top, \omega_m, \phi_m, u_{dc}, (i_f^{abc})^\top, \phi_g, \beta_\diamond \big)^\top \in \mathbb{R}^{11},
$$

and control input vector

$$
u := \Big(\underbrace{(u_1, u_2, u_3)}_{=:u_{1\text{-}3}^\top}, \underbrace{(u_4, u_5, u_6)}_{=:u_{4\text{-}6}^\top}, u_7 \Big)^\top := \big((u_{s,ref}^{abc})^\top, (u_{f,ref}^{abc})^\top, \beta_{ref} \big)^\top \in \mathbb{R}^7,
$$

the overall system dynamics with output y are given by the following nonlinear ordinary differential equation

$$\frac{\mathrm{d}}{\mathrm{d}t}\boldsymbol{x} = \underbrace{\begin{pmatrix} (\boldsymbol{L}_\mathrm{s}^{abc})^{-1}\left[x_6\boldsymbol{T}_\mathrm{vsc}\sigma\left(\frac{\boldsymbol{u}_{1\text{-}3}}{x_6/2} - \boldsymbol{1}_3 c_\wedge(t)\right) - R_\mathrm{s}\boldsymbol{x}_{1\text{-}3} + n_\mathrm{p}x_4\widehat{\psi}_\mathrm{pm}\begin{pmatrix}\sin(n_\mathrm{p}x_5)\\\sin(n_\mathrm{p}x_5 - \frac{2}{3}\pi)\\\sin(n_\mathrm{p}x_5 - \frac{4}{3}\pi)\end{pmatrix}\right] \\ \frac{1}{\Theta}\left[\varrho\,\pi\,r_\mathrm{t}^2\,v_\mathrm{w}(t)^3\frac{c_\mathrm{p}\left(r_\mathrm{t}x_4/(g_\mathrm{r}v_\mathrm{w}(t)),\,\mathrm{sat}_{0°}^{90°}(x_{11})\right)}{2x_4} + n_\mathrm{p}\widehat{\psi}_\mathrm{pm}\boldsymbol{x}_{1\text{-}3}^\top\boldsymbol{J}_\Sigma\begin{pmatrix}\cos(n_\mathrm{p}x_5)\\\cos(n_\mathrm{p}x_5 - \frac{2}{3}\pi)\\\cos(n_\mathrm{p}x_5 - \frac{4}{3}\pi)\end{pmatrix}\right] \\ x_4 \\ \frac{1}{C_\mathrm{dc}}\left[-\boldsymbol{x}_{1\text{-}3}^\top\sigma\left(\frac{\boldsymbol{u}_{1\text{-}3}}{x_6/2} - \boldsymbol{1}_3 c_\wedge(t)\right) - \boldsymbol{x}_{7\text{-}9}^\top\sigma\left(\frac{\boldsymbol{u}_{4\text{-}6}}{x_6/2} - \boldsymbol{1}_3 c_\wedge(t)\right)\right] \\ \frac{1}{L_\mathrm{f}}\left[x_6\boldsymbol{T}_\mathrm{vsc}\sigma\left(\frac{\boldsymbol{u}_{4\text{-}6}}{x_6/2} - \boldsymbol{1}_3 c_\wedge(t)\right) - R_\mathrm{f}\boldsymbol{x}_{7\text{-}9} - \hat{u}_\mathrm{g}(t)\begin{pmatrix}\cos(x_{10})\\\cos(x_{10} - \frac{2\pi}{3})\\\cos(x_{10} - \frac{4\pi}{3})\end{pmatrix}\right] \\ \omega_\mathrm{g}(t) \\ \mathrm{sat}_{-\beta_\mathrm{max}}^{\beta_\mathrm{max}}\left(\frac{1}{T_\beta}\left(-\mathrm{sat}_{0°}^{90°}(x_{11}) + u_7\right)\right) \end{pmatrix}}_{=:\boldsymbol{f}_\mathrm{abc}(\boldsymbol{x},\boldsymbol{u},t)\in\mathbb{R}^{11}}$$

$$\boldsymbol{y} = \underbrace{\hat{u}_\mathrm{g}(t)\begin{pmatrix}\cos(x_{10})\\\cos(x_{10} - \frac{2\pi}{3})\\\cos(x_{10} - \frac{4\pi}{3})\end{pmatrix}^\top\begin{bmatrix}\boldsymbol{I}_3\\\boldsymbol{J}_\Sigma\end{bmatrix}\boldsymbol{x}_{7\text{-}9}}_{=:\boldsymbol{h}_\mathrm{abc}(\boldsymbol{x},t)\in\mathbb{R}^2} = \begin{pmatrix}p_\mathrm{pcc}(\boldsymbol{i}_\mathrm{f}^{abc},t)\\q_\mathrm{pcc}(\boldsymbol{i}_\mathrm{f}^{abc},t)\end{pmatrix}$$

(17)

with initial values

$$\boldsymbol{x}(0) = \left((\boldsymbol{i}_\mathrm{s,0}^{abc})^\top, \omega_\mathrm{m,0}, \phi_\mathrm{m,0}, u_\mathrm{dc,0}, (\boldsymbol{i}_\mathrm{f,0}^{abc})^\top, \phi_\mathrm{g,0}, \beta_{\diamond,0}\right)^\top.$$

(18)

Note that, for brevity and clarity, the argument t is only shown for (purely time-varying) disturbances like wind $v_\mathrm{w}(\cdot)$, carrier signal $c_\wedge(\cdot)$ of modulator, grid amplitude $\hat{u}_\mathrm{g}(\cdot)$ and grid angular frequency $\omega_\mathrm{g}(\cdot)$.

3.3. Electrical System in (Simplified) Synchronously Rotating (d,q)-Reference Frame

Due to the star-connection of machine (stator) windings and grid-side network, the sums of stator and filter currents are zero for all time, i.e., $i_\mathrm{s}^a(t) + i_\mathrm{s}^b(t) + i_\mathrm{s}^c(t) = i_\mathrm{f}^a(t) + i_\mathrm{f}^b(t) + i_\mathrm{f}^c(t) = 0$ for all $t \geq 0$, respectively. Applying the Clarke-Park transformation (with transformation angle $\phi_\mathrm{p} = n_\mathrm{p}\phi_\mathrm{m}$ and $\phi_\mathrm{p} = \phi_\mathrm{g}$ on machine and grid side, resp.) to the machine-side and grid-side entries in (17) yields a representation of the respective models in the simplified synchronously rotating (d,q)-reference frame. To detect the grid voltage angle ϕ_g used in Clarke-Park transformation $\boldsymbol{T}_\mathrm{cp}(\phi_\mathrm{g})$, a phase-locked loop is usually used [60]. For details see [45,48].

3.3.1. Machine-Side Dynamics: Electrical Machine (Generator) and Drive Train

For permanent magnet flux linkage orientation, i.e., $\phi_\mathrm{p}(t) = n_\mathrm{p}\phi_\mathrm{m}(t)$, the PMSG dynamics simplify. The simplified PMSG dynamics in the (d,q)-reference frame are given by [45]

$$\frac{\mathrm{d}}{\mathrm{d}t}\boldsymbol{i}_\mathrm{s}^{dq}(t) = L_\mathrm{s}^{-1}\left[\boldsymbol{u}_\mathrm{s}^{dq}(t) - R_\mathrm{s}\boldsymbol{i}_\mathrm{s}^{dq}(t) - n_\mathrm{p}\omega_\mathrm{m}(t)\boldsymbol{J}\left(L_\mathrm{s}\boldsymbol{i}_\mathrm{s}^{dq}(t) + \underbrace{\begin{pmatrix}\frac{3}{2}\kappa\widehat{\psi}_\mathrm{pm}\\0\end{pmatrix}}_{=:\boldsymbol{\psi}_\mathrm{pm}^{dq}}\right)\right]$$

$$\frac{\mathrm{d}}{\mathrm{d}t}\omega_\mathrm{m}(t) = \frac{1}{\Theta}\left[\underbrace{\frac{m_\mathrm{t}\left(v_\mathrm{w}(t),\beta(t),\omega_\mathrm{m}(t)\right)}{g_\mathrm{r}} + n_\mathrm{p}\frac{2}{3\kappa^2}\boldsymbol{i}_\mathrm{s}^{dq}(t)^\top\boldsymbol{J}\boldsymbol{\psi}_\mathrm{pm}^{dq}}_{=:m_\mathrm{m}\left(\boldsymbol{i}_\mathrm{s}^{dq}(t)\right)}\right]$$

$$\frac{\mathrm{d}}{\mathrm{d}t}\phi_\mathrm{m}(t) = \omega_\mathrm{m}(t)$$

(19)

with initial values $i_s^{dq}(0) = T_{cp}(n_p\phi_m(0))i_{s,0}^{abc}$, $\omega_m(0) = \omega_{m,0}$ and $\phi_m(0) = \phi_{m,0}$, and overall stator inductance $L_s := \frac{3}{2}L_{s,m} + L_{s,\sigma}$. Note that, for the considered isotropic PMSG, the machine torque is independent of the d-current component and simplifies to [48] (p. 534)

$$m_m\big(i_s^{dq}\big) = m_m\big(i_s^q\big) = n_p\frac{2}{3\kappa^2}\frac{3}{2}\kappa\,\widehat{\psi}_{pm}i_s^q = \frac{n_p}{\kappa}\widehat{\psi}_{pm}i_s^q \implies i_{s,ref}^q = \frac{\kappa}{n_p\widehat{\psi}_{pm}}m_{m,ref} \text{ and } i_{s,ref}^d = 0, \quad (20)$$

which allows to compute the required reference currents $i_{s,ref}^d = 0$ (to reduce copper losses) and $i_{s,ref}^q$ for given reference torque $m_{m,ref}$ (in N m).

3.3.2. Power Electronics and DC-Link Dynamics (Back-to-Back Converter)

Note that, for all $\phi_p \in \mathbb{R}$, it holds

$$T_{cp}(\phi_p)^{-\top}T_{cp}(\phi_p)^{-1} = \frac{2}{3\kappa^2}I_2 \quad \text{and} \quad T_{cp}(\phi_p)T_{vsc} = T_{cp}(\phi_p). \quad (21)$$

Hence, the output voltages of the VSCs in the (d,q)-reference frame are given by $\forall\phi_p \in \{n_p\phi_m, \phi_g\} \; \forall z \in \{s, f\}$:

$$
\begin{aligned}
u_z^{dq} &:= T_{cp}(\phi_p)u_z^{abc}(s_z^{abc}, u_{dc}) \\
&\overset{(10),(21)}{=} u_{dc}T_{cp}(\phi_p)s_z^{abc} && (22) \\
&\overset{(12)}{=} u_{dc}T_{cp}(\phi_p)\sigma\Big(\frac{T_{cp}(\phi_p)^{-1}u_{z,ref}^{dq}}{u_{dc}/2} - \mathbf{1}_3c_\wedge(t)\Big), && (23)
\end{aligned}
$$

i.e., $u_z^{dq} = u_z^{dq}(u_{z,ref}^{dq}, u_{dc}, \phi_p)$. This allows to derive the DC-link dynamics as follows

$$
\begin{aligned}
\frac{d}{dt}u_{dc}(t) &\overset{(11)}{=} \frac{1}{C_{dc}}\Big(-i_s^{dq}(t)^\top T_{cp}\big(n_p\phi_m(t)\big)^{-\top}s_s^{abc}(t) - i_f^{dq}(t)^\top T_{cp}\big(\phi_g(t)\big)^{-\top}s_f^{abc}(t)\Big), \\
&\overset{(22),(21)}{=} \frac{1}{C_{dc}u_{dc}}\Big(\underbrace{-\frac{2}{3\kappa^2}i_s^{dq}(t)^\top u_s^{dq}(t)}_{=p_s(t)} \underbrace{-\frac{2}{3\kappa^2}i_f^{dq}(t)^\top u_f^{dq}(t)}_{=p_f(t)}\Big) \\
&\overset{(23)}{=} \frac{2}{3\kappa^2 C_{dc}}\Big(-i_s^{dq}(t)^\top T_{cp}(n_p\phi_m)\cdot\sigma\Big(\frac{T_{cp}(n_p\phi_m)^{-1}u_{s,ref}^{dq}}{u_{dc}/2} - \mathbf{1}_3c_\wedge(t)\Big) \\
&\qquad\qquad -i_f^{dq}(t)^\top T_{cp}(\phi_g)\cdot\sigma\Big(\frac{T_{cp}(\phi_g)^{-1}u_{f,ref}^{dq}}{u_{dc}/2} - \mathbf{1}_3c_\wedge(t)\Big)\Big).
\end{aligned} \quad (24)
$$

3.3.3. Grid-Side Dynamics (Filter, PCC, and Grid)

The grid-side dynamics also simplify. For grid voltage orientation, i.e., $\phi_p = \phi_g$, the grid-side system in the (d,q)-reference frame is given by [45]

$$\frac{d}{dt}i_f^{dq}(t) = \frac{1}{L_f}\Big[u_f^{dq}(t) - R_f i_f^{dq}(t) - \omega_g(t)L_f J i_f^{dq}(t) - \underbrace{\begin{pmatrix}\frac{3}{2}\kappa\,\widehat{u}_g(t)\\ 0\end{pmatrix}}_{=:u_g^{dq}(t)}\Big], \quad (25)$$

with initial value $i_f^{dq}(0) = T_{cp}(\phi_g(0))i_{f,0}^{abc} \in \mathbb{R}^2$.

3.3.4. Power Output

In the (d, q)-reference frame, active and reactive instantaneous powers p_{pcc} (in W) and q_{pcc} (in var) at the PCC simplify to ([48] and [49] (Chaper 14))

$$p_{pcc}(\boldsymbol{i}_f^{dq}, t) = \frac{2}{3\kappa^2} \boldsymbol{u}_g^{dq}(t)^\top \boldsymbol{i}_f^{dq} \overset{(25)}{=} \frac{1}{\kappa} \hat{u}_g(t) i_f^d \qquad \text{and}$$

$$q_{pcc}(\boldsymbol{i}_f^{dq}, t) = \frac{2}{3\kappa^2} \boldsymbol{u}_g^{dq}(t)^\top \boldsymbol{J} \boldsymbol{i}_f^{dq} \overset{(25)}{=} -\frac{1}{\kappa} \hat{u}_g(t) i_f^q, \qquad (26)$$

with $\boldsymbol{u}_g^{dq}$ and $\hat{u}_g$ as in (25) and $\kappa \in \{\frac{2}{3}, \sqrt{\frac{2}{3}}\}$.

3.3.5. Overall Dynamics in Nonlinear State-Space Representation

In the (d, q)-reference frame, the overall model is of 9th order. Note that switching is still considered. For (reduced) state vector

$$\boldsymbol{x} := \left(\underbrace{(x_1, x_2)}_{=:x_{1\text{-}2}^\top}, x_3, x_4, x_5, \underbrace{(x_6, x_7)}_{=:x_{6\text{-}7}^\top}, x_8, x_9 \right)^\top := \left((\boldsymbol{i}_s^{dq})^\top, \omega_m, \phi_m, u_{dc}, (\boldsymbol{i}_f^{dq})^\top, \phi_g, \beta_\Diamond \right)^\top \in \mathbb{R}^9, \quad (27)$$

and (reduced) control input

$$\boldsymbol{u} := \left(\underbrace{(u_1, u_2)}_{=:u_{1\text{-}2}^\top}, \underbrace{(u_3, u_4)}_{=:u_{3\text{-}4}^\top}, u_5 \right)^\top := \left((\boldsymbol{u}_{s,ref}^{dq})^\top, (\boldsymbol{u}_{f,ref}^{dq})^\top, \beta_{ref} \right)^\top \in \mathbb{R}^5, \qquad (28)$$

the overall (but reduced) nonlinear system dynamics with output are given by the following ninth-order ordinary differential equation

$$\frac{\mathrm{d}}{\mathrm{d}t} \boldsymbol{x} = \left(\begin{array}{c} \frac{1}{L_s} \left[x_5 \boldsymbol{T}_{cp}(n_p x_4) \sigma\left(\frac{\boldsymbol{T}_{cp}(n_p x_4)^{-1} u_{1\text{-}2}}{x_5/2} - \boldsymbol{1}_3 c_\wedge(t) \right) - R_s x_{1\text{-}2} - n_p x_3 \boldsymbol{J}\left(L_s x_{1\text{-}2} + \binom{\frac{3}{2}\kappa\hat{\psi}_{pm}}{0} \right) \right] \\[4mm] \frac{1}{\Theta} \left[\varrho\, \pi\, r_t^2\, v_w(t)^3 \frac{c_p\left(r_t x_3/(g_r v_w(t)), sat_{0^\circ}^{90^\circ}(x_9) \right)}{2 x_3} + \frac{n_p}{\kappa} \hat{\psi}_{pm} x_2 \right] \\[4mm] x_3 \\[3mm] \frac{2}{3\kappa^2 C_{dc}} \left[-x_{1\text{-}2}^\top \boldsymbol{T}_{cp}(n_p x_4) \cdot \sigma\left(\frac{\boldsymbol{T}_{cp}(n_p x_4)^{-1} u_{1\text{-}2}}{x_5/2} - \boldsymbol{1}_3 c_\wedge(t) \right) - x_{6\text{-}7}^\top \boldsymbol{T}_{cp}(x_{10}) \cdot \sigma\left(\frac{\boldsymbol{T}_{cp}(x_{10})^{-1} u_{3\text{-}4}}{x_5/2} - \boldsymbol{1}_3 c_\wedge(t) \right) \right] \\[4mm] \frac{1}{L_f} \left[x_5 \boldsymbol{T}_{cp}(x_{10}) \sigma\left(\frac{\boldsymbol{T}_{cp}(x_{10})^{-1} u_{3\text{-}4}}{x_5/2} - \boldsymbol{1}_3 c_\wedge(t) \right) - R_f x_{6\text{-}7} - \omega_g(t) L_f \boldsymbol{J} x_{6\text{-}7} - \binom{\frac{3}{2}\kappa\hat{u}_g(t)}{0} \right] \\[4mm] \omega_g(t) \\[2mm] sat_{-\beta_{max}}^{\beta_{max}} \left(\frac{1}{T_\beta} \left(-sat_{0^\circ}^{90^\circ}(x_9) + u_5 \right) \right) \end{array} \right)}_{=:f_{dq}(\boldsymbol{x}, \boldsymbol{u}, t) \in \mathbb{R}^9}$$

$$\boldsymbol{y} = \underbrace{\frac{1}{\kappa} \binom{\hat{u}_g(t)}{0}^\top \begin{bmatrix} \boldsymbol{I}_2 \\ \boldsymbol{J} \end{bmatrix} x_{6\text{-}7}}_{=:h_{dq}(\boldsymbol{x},t) \in \mathbb{R}^2} = \binom{p_{pcc}(\boldsymbol{i}_f^{dq}, t)}{q_{pcc}(\boldsymbol{i}_f^{dq}, t)}$$

$$(29)$$

with initial value

$$\boldsymbol{x}(0) = \left((\boldsymbol{T}_{cp}(n_p \phi_m(0)) \boldsymbol{i}_{s,0}^{abc})^\top, \omega_{m,0}, \phi_{m,0}, u_{dc,0}, (\boldsymbol{T}_{cp}(\phi_g(0)) \boldsymbol{i}_{f,0}^{abc})^\top, \phi_{g,0}, \beta_{\Diamond,0} \right)^\top.$$

Again, the argument t is only shown for wind $v_w(\cdot)$, modulator carrier signal $c_\wedge(\cdot)$, grid voltage amplitude $\hat{u}_g(\cdot)$ and grid angular frequency $\omega_g(\cdot)$. Note that, in view of the star connection on machine and grid side, the models (17) and (29) are equivalent.

4. Control Systems and Operation Management

4.1. Controllers

In this section, the individual controllers of the cascaded control system are described. In Section 6, the controllers will be used for the numerical simulation of the WTS models. The overall control system is shown in Figure 7 for the machine side and in Figure 8 for the grid side.
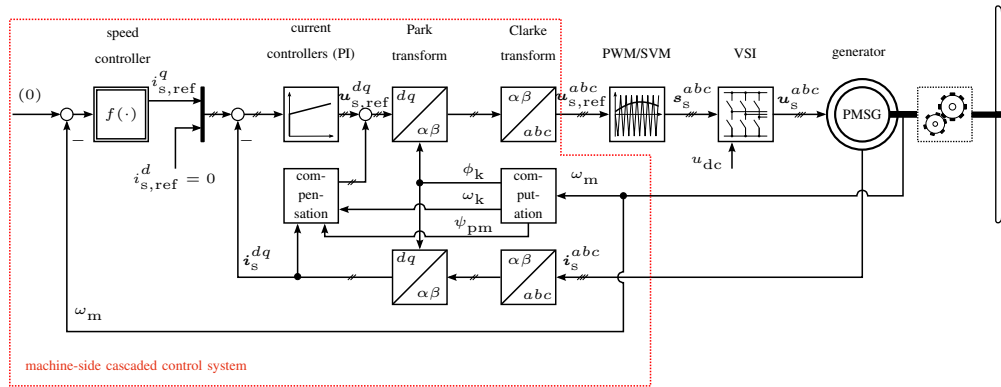

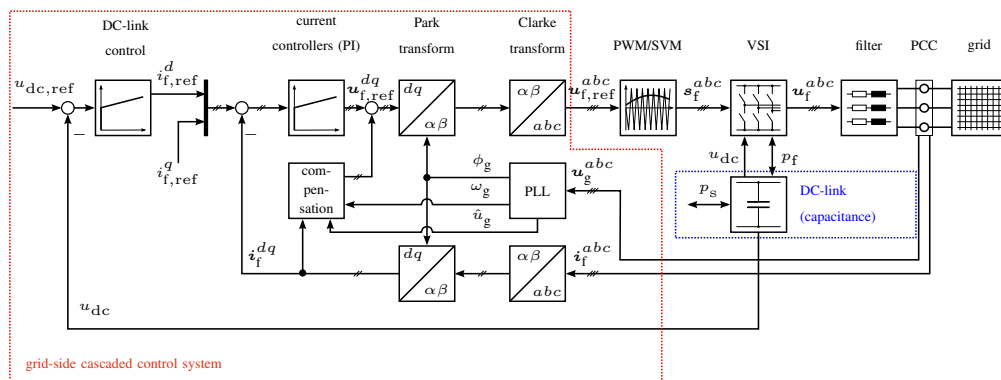**Figure 7.** Machine-side cascaded control system (Regime II).

Figure 8. Grid-side cascaded control system.

4.1.1. Machine-Side and Grid-Side Current Controllers ($z \in \{s, f\}$)

The current closed-loop systems on machine/stator ($z = s$) and grid/filter ($z = f$) side consist of two PI controllers (usually implemented in the (d, q)-reference frame), two disturbance compensation feedforward controllers, and the respective current dynamics as presented above. The applied control action consists of two parts, for $z \in \{s, f\}$, as follows

$$u_{z,\text{ref}}^{dq}(t) = \underbrace{u_{z,\text{pi}}^{dq}(t)}_{\text{PI controller output}} + \underbrace{u_{z,\text{comp}}^{dq}(t)}_{\text{disturbance compensation}}. \tag{30}$$

Details can be found in e.g., [63] (Section 7.1.1) or [45] (with similar notation as here). Hence, the voltage reference $u_{z,\text{ref}}^{dq} = (u_{z,\text{ref}}^d, u_{z,\text{ref}}^q)^\top$—the control input to the VSC—is the sum of the disturbance compensation $u_{z,\text{comp}}^{dq} = (u_{z,\text{comp}}^d, u_{z,\text{comp}}^q)^\top$ and the output $u_{z,\text{pi}}^{dq} = (u_{z,\text{pi}}^d, u_{z,\text{pi}}^q)^\top$ of the PI controller(s). The goal of the disturbance compensation is to obtain (almost) *decoupled* current

dynamics for controller design in the (d, q)-reference frame. Therefore, depending on the application, the coupling terms [45,64] are, for $z \in \{s,f\}$, given by

$$
\boldsymbol{u}_{z,\text{dist}}^{dq}(t) := \begin{cases} -n_p \omega_m(t) \boldsymbol{J} \big(L_s \boldsymbol{i}_s^{dq}(t) + \boldsymbol{\psi}_{pm}^{dq} \big), & \text{for PMSGs as in (19)} \\ -\omega_g(t) L_f \boldsymbol{J} \boldsymbol{i}_f^{dq}(t) - \boldsymbol{u}_g^{dq}(t), & \text{for RL-filter \& grid as in (25),} \end{cases} \tag{31}
$$

which can be (roughly) compensated for by introducing the following feedforward control action $\boldsymbol{u}_{z,\text{comp}}^{dq} = -\boldsymbol{u}_{z,\text{dist}}^{dq}$.

It is well known that PI(D) controllers in presence of input saturation may exhibit integral windup (in particular for large initial errors) leading to large overshoots and/or oscillations in the closed-loop system response (see, e.g., [65,66]). Due to the limited DC-link voltage u_{dc} (in V), the output of the VSC is constrained by the saturation level

$$
\widehat{u}(u_{dc}) \in \big[\tfrac{u_{dc}}{2}, \tfrac{2u_{dc}}{3} \big] \tag{32}
$$

(in V) which depends on the employed modulation strategy (such as pulse-width modulation (PWM) or space-vector modulation (SVM) with or without over-modulation [54] (Section 8.4)).

Due to the input saturation, a simple but effective anti-windup strategy (There exists a variety of anti-windup strategies. For this paper, the simple and popular conditional integration technique was chosen. Any other approach seems also feasible.) (similar to *conditional integration*) is implemented. To do so, the transition function $f_{\widehat{u}, \Delta_{\xi_z}}(\cdot)$ as in (49) is combined with the two-input two-output PI controller

$$
\left.\begin{aligned} \tfrac{d}{dt} \boldsymbol{\xi}_z^{dq}(t) &= f_{\widehat{u}, \Delta_{\xi_z}} \big(\| \boldsymbol{u}_{z,\text{ref}}^{dq}(t) \| \big) \, \boldsymbol{e}_z^{dq}(t), \\ \boldsymbol{u}_{z,\text{pi}}^{dq}(t) &= k_{z,p} \boldsymbol{e}_z^{dq}(t) + k_{z,i} \boldsymbol{\xi}_z^{dq}(t), \end{aligned}\right\} \tag{33}
$$

where $\boldsymbol{\xi}_z^{dq}(0) = \boldsymbol{\xi}_{z,0}^{dq} \in \mathbb{R}^2$ is the initial value, $\boldsymbol{\xi}_z^{dq} = (\xi_z^d, \xi_z^q)^\top$ is the integrator output vector of the PI controllers, and $\boldsymbol{e}_z^{dq} = (e_z^d, e_z^q)^\top = \boldsymbol{i}_{z,\text{ref}}^{dq} - \boldsymbol{i}_z^{dq}$ is the current tracking error, Δ_{ξ_z} is the transition interval during which anti-windup already becomes active in [48] (Section 14.4) ($z \in \{s,f\}$). The parameters $k_{z,p}$ and $k_{z,i}$ are the proportional and integral controller gain, respectively. The controller gains can be tuned, e.g., according to the "Magnitude Optimum criterion" (i.e., $k_{z,p} = L_z/(2T_{\text{avg}})$ and $k_{z,i} = R_z/(2T_{\text{avg}})$; see [45,67]) or any other convenient/preferred tuning rule.

4.1.2. Speed Controller (Regime II)

For wind speeds below the nominal wind speed, maximum power point tracking is the desired control objective (cf. Figure 2). The following nonlinear controller, given by

$$
m_{m,\text{ref}}(t) = -\text{sat}_0^{\overline{m}_m} \big[k_p^\star \omega_m(t)^2 \big] \quad \text{where} \quad k_p^\star := \frac{\varrho \pi r_t^5}{2 g_r^3} \frac{c_p(\lambda^\star, \beta^\star)}{(\lambda^\star)^3}, \tag{34}
$$

achieves maximum power point tracking even without wind speed measurement (This implies a perfectly working torque control. If this assumption does not hold, this might impact WTS efficiency and power production [68].). The controller (34) requires knowledge of the optimal tip speed ratio $\lambda^\star$ and optimal pitch angle $\beta^\star \geq 0$ for the turbine to extract the maximum available wind power. Moreover, its output is saturated by $\overline{m}_m$ (e.g., by the nominal/rated machine torque). In ref. [69], for a constant wind speed $v_w > 0$, it has been shown that the speed closed-loop system (neglecting the underlying current closed-loop system and the pitch control system, i.e., $m_{m,\text{ref}} = m_m$ and $\beta = \beta^\star$) is stable and the optimal tip speed ratio $\lambda^\star$ (or the optimal speed $\omega_m^\star = \lambda^\star \frac{v_w}{r_t}$) is reached asymptotically.

4.1.3. Torque Controller and Pitch Reference Controller (Regime III)

When the wind speed exceeds the nominal wind speed of the turbine, i.e., $v_\text{w} > v_\text{w,rated}$, the WTS operates in regime III where the rotor/machine speed is controlled indirectly by the pitch control system and the machine-side torque control system outputs the nominal generator torque (cf. Figure 2). The pitch control system allows to reduce the turbine torque (independently of the wind). To reduce mechanical stress, a smooth (continuous) transition between regime II and regime III is crucial which can be established by introducing an outer pitch reference controller cascade which adjusts the pitch angle reference β_ref appropriately. Here, an output-saturated PI controller with anti-windup is proposed. Its nonlinear dynamics are given by

$$\left.\begin{aligned}
\frac{\mathrm{d}}{\mathrm{d}t}\xi_\beta(t) &= f_{0°,\Delta_{\xi_\beta}}\Big(-k_{\beta,\text{p}}\big(\overbrace{\omega_\text{m,rated}-\omega_\text{m}(t)}^{=:e_{\omega_\text{m}}(t)}\big)-k_{\beta,\text{i}}\xi_\beta(t)\Big)\,e_{\omega_\text{m}}(t), \\
\beta_\text{ref}(t) &= \mathrm{sat}_{0°}^{90°}\big[k_{\beta,\text{p}}e_{\omega_\text{m}}(t)+k_{\beta,\text{i}}\xi_\beta(t)\big]
\end{aligned}\right\} \tag{35}$$

with initial value $\xi_\beta(0)=\xi_{\beta,0}$. The dynamics depend on speed error $e_\omega := \omega_\text{m,rated}-\omega_\text{m}$, integrator state ξ_β with anti-windup transition function $f_{0°,\Delta_{\xi_\beta}}(\cdot)$ as in (49) (with $\hat{a}=0°$ and $\Delta=\Delta_{\xi_\beta}>0$), proportional gain $k_{\beta,\text{p}}>0$ and integrator gain $k_{\beta,\text{i}}>0$. Note that the output β_ref of the PI controller is saturated to the interval $[0°,90°]$. Figure 9 shows the block diagram of the nonlinear PI controller implementation.
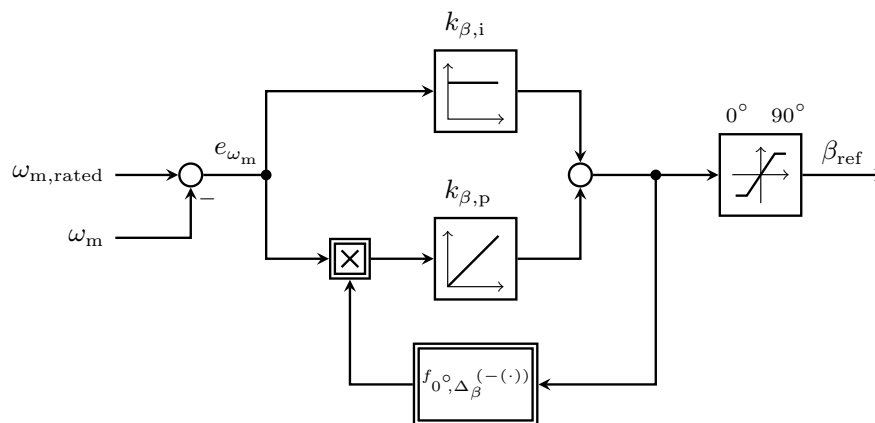

Figure 9. Nonlinear pitch reference PI controller.

4.1.4. DC-Link Voltage Controller and Reactive Power Feedforward Controller

On the grid side, active and reactive power can be fed into the grid. The active power is indirectly controlled by the DC-link voltage controller via the d-component of the grid-side currents, whereas the reactive power is controlled by a simple feedforward controller via the q-component of the filter current. DC-link voltage control is a non-trivial task, since the DC-link system dynamics might exhibit a non-minimum phase behavior. Therefore, some care must be exercised during controller tuning leading to a rather conservative design (for more details see [45,70,71]). In most cases, a PI controller is implemented for DC-link voltage control. Such a PI controller with anti-windup is given by

$$\left.\begin{aligned}
\frac{\mathrm{d}}{\mathrm{d}t}\xi_\text{dc}(t) &= f_{\hat{\imath},\Delta_{\xi_\text{dc}}}\big(\|\boldsymbol{i}_\text{f,ref}^{dq}(t)\|\big)\,\big(\overbrace{u_\text{dc,ref}(t)-u_\text{dc}(t)}^{=:e_\text{dc}(t)}\big), \\
i_\text{f,ref}^d(t) &= k_\text{dc,p}e_\text{dc}(t)+k_\text{dc,i}\,\xi_\text{dc}(t),
\end{aligned}\right\} \tag{36}$$

where $\xi_\text{dc}(0)=\xi_{\text{dc},0}\in\mathbb{R}$ is the initial value and $f_{\hat{\imath},\Delta_{\xi_\text{dc}}}(\cdot)$ is as in ref. (49), $\hat{\imath}$ is the maximally admissible filter current amplitude (e.g., nominal current) and Δ_{ξ_dc} is the transition interval for

anti-windup. For given reactive power reference $q_{\text{pcc,ref}}$ (provided e.g., by the grid operator), the grid-side reference q-current

$$i_{\text{f,ref}}^q(t) = -\kappa \frac{q_{\text{pcc,ref}}(t)}{\widehat{u}_{\text{g}}(t)} \tag{37}$$

can be obtained by rearranging (26) and can be used to feedforward control the desired reactive power.

4.2. Operation Management

The operation management is the high-level control system of the WTS (see Figure 1). Based on the measured wind speed $\widehat{v}_{\text{w}}$ (rough estimate of the actually incoming wind speed v_{w}), it aligns the rotor perpendicular to the wind direction (i.e., yawing; not considered in this paper) and it commands the transitions between the four operation regimes. For example, it triggers startup (transition between regime I $\rightarrow$ regime II or regime IV $\rightarrow$ regime III) or shutdown (transition between regime II $\rightarrow$ regime I or regime III $\rightarrow$ regime IV). Moreover, the operation management is the link between single WTSs and the wind park management system or the system operator. It receives reference values for reactive (in the future, also active) power and propagates them to the underlying control system. Additionally, it also might provide the DC-link voltage reference $u_{\text{dc,ref}}$ for the back-to-back converter or decides wether to perform an emergency shutdown to protect the WTS.

5. Reduced-Order Models

The presented WTS models in Section 3 consider all relevant dynamic effects and switching of the power electronic devices. The dynamic models are of eleventh and ninth order for the (a, b, c)- and the (d, q)-reference frame, respectively, and involve a high complexity with respect to computation and control design. Hence, for many studies concerning large-scale power systems [4,5,13,22] or high-level controller design of renewable energy systems for contributing in frequency and voltage stability [18], these detailed models are not a viable option. Thus, in this section, two models with reduced complexity are developed. In contrast to existing low-complexity WTS models [22,26,32,43,72], the model reduction in this paper follows a systematic step by step procedure with well-founded simplification assumptions.

5.1. Non-Switching Model (Nsm) or Averaging Model

In a first simplification step, the explicit switching of the power electronics is neglected. The voltages applied on machine ($z = s$) and grid side ($z = f$) by the power electronics can be assumed to be equal to the averaged but saturated output phase voltage vector $\boldsymbol{u}_{\text{z}}^{abc}(t) = \mathbf{sat}_{\widehat{u}}(\overline{\boldsymbol{u}}_{\text{z}}^{abc}(t)) \approx \mathbf{sat}_{\widehat{u}}(\boldsymbol{u}_{\text{z,ref}}^{abc}(t - T_{\text{avg}}))$ with $\widehat{u} = \widehat{u}(u_{\text{dc}})$ as in (32) (see also (10) and (14) in Section 3.2.2 for a definition of the saturation function $\mathbf{sat}_{\widehat{u}}(\cdot)$). Moreover, in comparison to the other dynamics of the WTS, the time constant T_{avg} is negligible (as of in the range of microseconds) finally leading to the simplification $\boldsymbol{u}_{\text{z}}^{abc}(t) = \mathbf{sat}_{\widehat{u}}(\boldsymbol{u}_{\text{z,ref}}^{abc}(t))$ which can be written as $\boldsymbol{u}_{\text{z}}^{dq}(t) = \mathbf{sat}_{\widehat{u}}(\boldsymbol{u}_{\text{z,ref}}^{dq}(t))$ in the (d, q)-reference frame (neglecting cross-coupling terms due to the Park transformation [48] (p. 521)). Consequently, the power electronics apply instantaneously the requested but possibly saturated voltages. Now, the resultant *non-switching model* can be introduced. Its state and control input vector are

$$\boldsymbol{x} := \big(\underbrace{(x_1, x_2)}_{=: \boldsymbol{x}_{1\text{-}2}^\top}, x_3, x_4, x_5, \underbrace{(x_6, x_7)}_{=: \boldsymbol{x}_{6\text{-}7}^\top}, x_8, x_9\big)^\top := \big((\boldsymbol{i}_{\text{s}}^{dq})^\top, \omega_{\text{m}}, u_{\text{dc}}, (\boldsymbol{i}_{\text{f}}^{dq})^\top, \beta_{\Diamond}\big)^\top \in \mathbb{R}^7, \tag{38}$$

and

$$\boldsymbol{u} := \big(\underbrace{(u_1, u_2)}_{=: \boldsymbol{u}_{1\text{-}2}^\top}, \underbrace{(u_3, u_4)}_{=: \boldsymbol{u}_{3\text{-}4}^\top}, u_5\big)^\top := \big((\boldsymbol{u}_{\text{s,ref}}^{dq})^\top, (\boldsymbol{u}_{\text{f,ref}}^{dq})^\top, \beta_{\text{ref}}\big)^\top \in \mathbb{R}^5, \tag{39}$$

respectively. Its nonlinear dynamics with output are given by

$$
\frac{\mathrm{d}}{\mathrm{d}t}\boldsymbol{x} = \begin{pmatrix}
L_\mathrm{s}^{-1}\left[\, \mathbf{sat}_{\hat{u}(x_4)}(\boldsymbol{u}_{1\text{-}2}) - R_\mathrm{s}\boldsymbol{x}_{1\text{-}2}(t) - n_\mathrm{p}x_3\boldsymbol{J}\left(L_\mathrm{s}\boldsymbol{x}_{1\text{-}2} + \begin{pmatrix}\frac{3}{2}\kappa\hat{\psi}_\mathrm{pm}\\0\end{pmatrix}\right)\right] \\[2ex]
\frac{1}{\Theta}\left[\varrho\,\pi\,r_\mathrm{t}^2\,v_\mathrm{w}(t)^3\dfrac{c_\mathrm{p}\left(r_\mathrm{t}x_3/(g_\mathrm{r}v_\mathrm{w}(t)),\mathrm{sat}_{0°}^{90°}(x_9)\right)}{2x_3} + \frac{n_\mathrm{p}}{\kappa}\hat{\psi}_\mathrm{pm}x_2\right] \\[2ex]
\frac{2}{3\kappa^2\,C_\mathrm{dc}x_4}\left[\,-\boldsymbol{x}_{1\text{-}2}^\top\,\mathbf{sat}_{\hat{u}(x_4)}(\boldsymbol{u}_{1\text{-}2}) - \boldsymbol{x}_{6\text{-}7}^\top\,\mathbf{sat}_{\hat{u}(x_4)}(\boldsymbol{u}_{3\text{-}4})\right] \\[2ex]
\frac{1}{L_\mathrm{f}}\left[\,\mathbf{sat}_{\hat{u}(x_4)}(\boldsymbol{u}_{3\text{-}4}) - R_\mathrm{f}\boldsymbol{x}_{6\text{-}7} - \omega_\mathrm{g}(t)L_\mathrm{f}\boldsymbol{J}\boldsymbol{x}_{6\text{-}7} - \begin{pmatrix}\frac{3}{2}\kappa\,\hat{u}_\mathrm{g}(t)\\0\end{pmatrix}\right] \\[2ex]
\mathrm{sat}_{-\dot{\beta}_\mathrm{max}}^{\dot{\beta}_\mathrm{max}}\left(\frac{1}{T_\beta}\left(-\mathrm{sat}_{0°}^{90°}(x_9) + u_5\right)\right)
\end{pmatrix}}_{=:\,f_\mathrm{nsm}(\boldsymbol{x},\boldsymbol{u},t)\,\in\,\mathbb{R}^7}
$$

$$
\boldsymbol{y} = \underbrace{\frac{1}{\kappa}\begin{pmatrix}\hat{u}_\mathrm{g}(t)\\0\end{pmatrix}^\top\begin{bmatrix}\boldsymbol{I}_2\\\boldsymbol{J}\end{bmatrix}\boldsymbol{x}_{6\text{-}7}}_{=:\,h_\mathrm{nsm}(\boldsymbol{x},t)\,\in\,\mathbb{R}^2} = \begin{pmatrix}p_\mathrm{pcc}(\boldsymbol{i}_\mathrm{f}^{dq},t)\\q_\mathrm{pcc}(\boldsymbol{i}_\mathrm{f}^{dq},t)\end{pmatrix}. \tag{40}
$$

As before, the argument t is only shown for disturbance signals such as wind $v_\mathrm{w}(\cdot)$ and grid voltage amplitude $\hat{u}_\mathrm{g}(\cdot)$. Note that the (transformation) angles ϕ_m and ϕ_g are not needed for this WTS model. Compared to the detailed model (29) in the (d,q)-reference frame, the non-switching model (40) is of seventh order and does not cover switching. As will be shown in Section 6, the simulation time and computational complexity of the non-switching model (40) reduces by several orders of magnitude compared to the simulation time of the detailed model (29) (in particular due to the neglected switching).

Remark 3. *The average voltage dynamics could also be considered and are often approximated by a saturated first order-lag system of the following form [48] (Chaper 14)*

$$
\forall z \in \{s,f\}: \quad \frac{\mathrm{d}}{\mathrm{d}t}\boldsymbol{u}_\mathrm{z}^{dq} = \frac{1}{T_\mathrm{avg}}\,\boldsymbol{sat}_{\hat{u}}\left(-\boldsymbol{u}_\mathrm{z}^{dq} + \boldsymbol{u}_\mathrm{z,ref}^{dq}\right)
$$

with initial value $\boldsymbol{u}_\mathrm{z}^{dq}(0) = \boldsymbol{0}_2$.

5.2. Reduced-Order Model (ROM)

In the next simplification step, no switching will be considered and only the dominant dynamics in (40) are identified. Hence, those dynamics will be neglected, which do not significantly contribute to the electrical power output of the WTS. In physical systems, the dynamics are related to the intrinsic energy storages in the system [73]. Considering the non-switching model (40) at its nominal (steady state) working point $p_\mathrm{t} = 2\,\mathrm{MW}$ (cf. [45] and Table 1), the following stored energies can be computed: $\frac{1}{2}\Theta\omega_\mathrm{m}^2 \approx 23\,960\,\mathrm{kJ}$, $\frac{1}{2}C_\mathrm{dc}u_\mathrm{dc}^2 \approx 349.92\,\mathrm{kJ}$, $\frac{1}{2}\frac{2}{3\kappa^2}L_\mathrm{s}^q\,(i_\mathrm{s}^q)^2 \approx 2.1\,\mathrm{kJ}$ (The factor $\frac{1}{2}\frac{2}{3\kappa^2}$ is due to the Clarke transformation factor $\kappa \in \{\frac{2}{3},\sqrt{\frac{2}{3}}\}$ which scales electrical power and energy by $\frac{2}{3\kappa^2}$ [48] (p. 510).), and $\frac{1}{2}\frac{2}{3\kappa^2}L_\mathrm{f}\,\|\boldsymbol{i}_\mathrm{f}^{dq}\|^2 \approx 4.39\,\mathrm{kJ}$, which gives the following energy relations for all wind speeds satisfying $v_\mathrm{w} \geq v_\mathrm{w,cut-in}$:

$$
\tfrac{1}{2}\Theta\omega_\mathrm{m}^2 \gg \tfrac{1}{2}C_\mathrm{dc}u_\mathrm{dc}^2 \gg \tfrac{1}{2}\tfrac{2}{3\kappa^2}L_\mathrm{f}\|\boldsymbol{i}_\mathrm{f}^{dq}\|^2 \approx \tfrac{1}{2}\tfrac{2}{3\kappa^2}L_\mathrm{s}^q\,(i_\mathrm{s}^q)^2.
$$

This comparison of the energy contents shows that, the energies stored in the inductances of the generator and filter are rather small compared to the kinetic energy and the DC-link energy. In other words, in the reduced representation, the electrical dynamics of generator and filter will not be modeled

explicitly anymore. The electrical dynamics of the currents, their current control loops with underlying VSCs are neglected. This implies that (i) the actual currents can be considered to equal their respective reference currents and (ii) the actual torque equals its reference value, i.e.,

$$i_s^{dq} = i_{s,ref}^{dq}, \quad i_f^{dq} = i_{f,ref}^{dq} \quad \text{and} \quad m_m = m_{m,ref} \quad \text{in (29) or (40), resp.} \tag{41}$$

Therefore, the reduced-order model has only a three-dimensional state vector

$$x := (x_1,\ x_2,\ x_3)^\top = (\omega_m,\ u_{dc},\ \beta_\diamond)^\top \in \mathbb{R}^3 \tag{42}$$

comprising angular velocity ω_m, DC-link voltage u_{dc} and pitch angle $\beta_\diamond$. The control input vector

$$u := \left(u_1, \underbrace{(u_2,\ u_3)}_{=:u_{2\text{-}3}^\top},\ u_4\right)^\top = \left(m_{m,ref},\ (i_{f,ref}^{dq})^\top, \beta_{ref}\right)^\top \in \mathbb{R}^4 \tag{43}$$

of the reduced-order model consists of the reference signals above and the reference pitch angle β_{ref}. Note that the four reference values come from the speed controller (34), the DC-link voltage controller (36), the reactive power (feedforward) controller (37) and the pitch controller (35), respectively, as introduced in Section 4.1.

Although the generator and filter dynamics are negligible, the resistive losses on machine and grid side should still be considered, since those scale with the squared current magnitude, i.e.,

$$p_{R_s} := \frac{2}{3\kappa^2} R_s \|i_s^{dq}\|^2 = \frac{2}{3\kappa^2} R_s \|i_{s,ref}^{dq}\|^2 \overset{(20)}{=} \frac{2R_s}{3n_p^2 \hat{\psi}_{pm}^2} m_{m,ref}^2, \tag{44}$$

$$p_{R_f} := \frac{2}{3\kappa^2} R_f \|i_f^{dq}\|^2 = \frac{2}{3\kappa^2} R_f \|i_{f,ref}^{dq}\|^2, \tag{45}$$

respectively. Note that the stator losses can be expressed by a nonlinear function of the reference torque instead of the stator currents. The copper losses in (45) will be included into the DC-link dynamics (11) as follows

$$
\begin{aligned}
\frac{d}{dt} u_{dc} &\overset{(40)}{=} \frac{2}{3\kappa^2 C_{dc} u_{dc}} \left[-(i_s^{dq})^\top \mathbf{sat}_{\hat{u}}(u_{s,ref}^{dq}) - (i_f^{dq})^\top \mathbf{sat}_{\hat{u}}(u_{f,ref}^{dq}) \right] \\
&\overset{(24)}{\approx} \frac{2}{3\kappa^2 C_{dc} u_{dc}} \left[-(i_s^{dq})^\top u_s^{dq} - (i_f^{dq})^\top u_f^{dq} \right] \\
&\overset{(19),(25)}{=} \frac{2}{3\kappa^2 C_{dc} u_{dc}} \left[-(i_s^{dq})^\top (R_s i_s^{dq} + n_p \omega_m J \psi_{pm}^{dq}) - (i_f^{dq})^\top \left(R_f i_f^{dq} + \begin{pmatrix} \frac{3}{2}\kappa \hat{u}_g(t) \\ 0 \end{pmatrix}\right) \right] \\
&= \frac{2}{3\kappa^2 C_{dc} u_{dc}} \left[-\left(R_s \|i_s^{dq}\|^2 + \underbrace{n_p \omega_m (i_s^{dq})^\top J \psi_{pm}^{dq}}_{\overset{(19)}{=} \frac{3\kappa^2}{2} \omega_m m_m}\right) - \left(R_f \|i_f^{dq}\|^2 + \frac{3}{2}\kappa \hat{u}_g(t) i_f^d\right) \right],
\end{aligned}
\tag{46}
$$

where, in the second to last step, (19) and (25) were solved for u_s^{dq} and u_f^{dq}, respectively, and the results were inserted into (46) while $(i_s^{dq})^\top J i_s^{dq} = 0$, $(i_f^{dq})^\top J i_f^{dq} = 0$ and the derivative terms with $\frac{d}{dt} i_s^{dq}$ and $\frac{d}{dt} i_f^{dq}$ were neglected (recall motivation above).

Table 1. List of system parameters used for simulations.

Description	Symbol	Value
Turbine & gear (direct drive)		
Air density	ϱ	$1.293\,\frac{\text{kg}}{\text{m}^3}$
Turbine radius	r_t	$40\,\text{m}$
Turbine inertia	Θ_t	$8.6 \times 10^6\,\text{kg}\,\text{m}^2$
Power coefficient	$c_{\text{p},2}(\cdot,\cdot)$	as in (4)
Maximal change rate of pitch angle	$\dot{\beta}_\text{max}$	$8\,\frac{\circ}{\text{s}}$
Pitch control time constant	T_β	$0.5\,\text{s}$
Gear ratio	g_r	1
Permanent magnet synchronous generator (isotropic)		
Number of pole pairs	n_p	48
Stator resistance	R_s	$0.01\,\Omega$
Stator inductance(s)	$L_\text{s}^d = L_\text{s}^q$	$3.0\,\text{mH}$
Permanent magnet flux	ψ_pm	$12.9\,\text{V}\,\text{s}$
Generator inertia	Θ_m	$1.3 \times 10^6\,\text{kg}\,\text{m}^2$
Back-to-back converter		
DC-link capacitance	C_dc	$2.4\,\text{mF}$
Switching frequency	f_sw	$2.5\,\text{kHz}$
Delay	$T_\text{delay} = \frac{1}{f_\text{sw}}$	$0.4\,\text{ms}$
Filter & grid voltage		
Filter resistance	R_f	$0.1\,\Omega$
Filter inductance	L_f	$6\,\text{mH}$
Grid angular frequency	$\omega_\text{g} = 2\pi f_\text{g}$	$100\pi\,\frac{\text{rad}}{\text{s}}$
Grid voltage amplitude	$\hat{u}_\text{g}$	$2.7\,\text{kV}$
Grid voltage initial angle	α_0	$0\,\text{rad}$
Controller parameters		
PI current controller (33)	$k_\text{f,p}$	$7.5\,\Omega$
(grid-side)	$k_\text{f,i}$	$125\,\Omega\,\text{s}$
	Δ_{ξ_f}	$1 \times 10^{-3}\,\text{V}$
	$\hat{u}$	$\frac{u_\text{dc}}{\sqrt{3}}$
PI current controller (33)	$k_\text{s,p}$	$3.75\,\Omega$
(machine-side)	$k_\text{s,i}$	$12.5\,\Omega\,\text{s}$
	Δ_{ξ_s}	$1 \times 10^{-3}\,\text{V}$
	$\hat{u}$	$\frac{u_\text{dc}}{\sqrt{3}}$
Speed controller (34)	$k_\text{p}^\star$	$282.80\,\frac{\text{kN}\,\text{m}}{\text{s}^2}$
	$m_\text{m,rated}$	$1.041\,9\,\text{MN}\,\text{m}$
DC-link voltage	$k_\text{dc,p}$	$-0.576\,\frac{\text{A}}{\text{V}}$
PI controller (36)	$k_\text{dc,i}$	$-18.33\,\frac{\text{A}\,\text{s}}{\text{V}}$
Phased-locked loop	$V_\text{r,pll}$	$20\,000\,\frac{1}{\text{s}}$
PI controller as in [45]	$T_\text{n,pll}$	$0.2\,\text{ms}$
Pitch angle reference	$k_{\beta,\text{p}}$	$-400.2\,\frac{\circ\,\text{s}}{\text{rad}}$
PI controller (35)	$k_{\beta,\text{i}}$	$-100.1\,\frac{\circ\,\text{s}^2}{\text{rad}}$
	Δ_{ξ_β}	$1 \times 10^{-3\circ}$
	$\omega_\text{m,rated}$	$1.919\,5\,\frac{\text{rad}}{\text{s}}$

Finally, by recalling state vector (42) and control input vector (43), and invoking (41), (47) and (45), the nonlinear state-space representation of the reduced-order model with output is obtained as

$$
\frac{\mathrm{d}}{\mathrm{d}t}\boldsymbol{x} = \underbrace{\begin{pmatrix} \frac{1}{\Theta}\left[\varrho\,\pi\,r_{\mathrm{t}}^2\,v_{\mathrm{w}}(t)^3 \cdot \frac{c_{\mathrm{P}}\left(r_{\mathrm{t}}x_1/(g_{\mathrm{r}}v_{\mathrm{w}}(t)),\mathrm{sat}_{0^\circ}^{90^\circ}(x_3)\right)}{2x_1} + u_1\right] \\[2mm] \frac{1}{C_{\mathrm{dc}}x_2}\left[-\underbrace{x_1\,u_1}_{\overset{(7)}{=}\,p_{\mathrm{m}}=p_{\mathrm{t}}<0} - \frac{2R_{\mathrm{s}}}{3n_{\mathrm{p}}^2\hat{\psi}_{\mathrm{pm}}^2}\,u_2^2 - \underbrace{\frac{1}{\kappa}\hat{u}_{\mathrm{g}}(t)\,u_2}_{\overset{(26)}{=}\,p_{\mathrm{pcc}}(i_{\mathrm{f}}^d,t)} - \frac{2}{3\kappa^2}R_{\mathrm{f}}\,\|\boldsymbol{u}_{2\text{-}3}\|^2\right] \\[2mm] \mathrm{sat}_{-\dot{\beta}_{\max}}^{\dot{\beta}_{\max}}\left(\frac{1}{T_\beta}\left(-\mathrm{sat}_{0^\circ}^{90^\circ}(x_3)+u_4\right)\right) \end{pmatrix}}_{=:\boldsymbol{f}_{\mathrm{rom}}(\boldsymbol{x},\boldsymbol{u},t)\in\mathbb{R}^3}
$$
$$
\boldsymbol{y} = \underbrace{\frac{1}{\kappa}\begin{pmatrix} \hat{u}_{\mathrm{g}}(t) \\ 0 \end{pmatrix}^\top \begin{bmatrix} \boldsymbol{I}_2 \\ \boldsymbol{J} \end{bmatrix}\boldsymbol{u}_{2\text{-}3}}_{=:\boldsymbol{h}_{\mathrm{rom}}(\boldsymbol{u},t)\in\mathbb{R}^2} \overset{(26),(41)}{=} \begin{pmatrix} p_{\mathrm{pcc}}(i_{\mathrm{f,ref}}^d,t) \\ q_{\mathrm{pcc}}(i_{\mathrm{f,ref}}^q,t) \end{pmatrix}
$$

$$(47)$$

with initial values $\boldsymbol{x}(0) = (\omega_{\mathrm{m},0},\, u_{\mathrm{dc},0},\, \beta_{\Diamond,0})^\top$. Note that via the DC-link dynamics the mechanical power $p_{\mathrm{m}} = p_{\mathrm{t}} = \omega_{\mathrm{m}}m_{\mathrm{m,ref}} < 0$ (minus the copper losses) is transfered to the PCC, whereas the active power p_{pcc} is induced. Again, only wind speed $v_{\mathrm{w}}(\cdot)$ and grid voltage amplitude $\hat{u}_{\mathrm{g}}(\cdot)$ are considered as time-varying disturbance signals. The reduced-order model (47) is of third order. Hence, compared to (40), six state variables are additionally eliminated, which reduces the computation and simulation time further (see Section 6). The controllers (34)–(37) presented in Section 4.1 can still be used as controllers of the reduced-order model(s).

6. Implementation and Comparative Simulations

In this section, the full-order model (29) from Section 3.3.5, the non-switching model (40) from Section 5.1 and the reduced-order model (47) from Section 5.2 were implemented in Matlab/Simulink (for details see Table 2). Note that, due to the equivalence of the full-order models (17) and (29), only the model in the synchronously rotating reference frame is implemented.

The comparative simulation results of all three implementations are shown in Figures 10–12. The results will be discussed in the following. The implementations were performed exactly based on the derived state space models described in the respective sections. The implementation parameters are listed in Table 1. The wind data used was measured at the FINO1 research platform ($54°\,00'\,53,5''$ N, $06°\,35'\,15,5''$ E) on the 23rd of September 2009 between 8:10–08:20 a.m. (with a time resolution of 10 Hz). In all Figures 10–12, the wind speed profile is shown in the upper most subplot. It is varying around the nominal wind speed (under- and overshooting) leading to an operation of the WTS in regime II *and* regime III. In order to achieve a fair comparison, all models are implemented with identical controllers and tuning for pitch angle β, DC-link voltage u_{dc} and angular velocity ω_{m} (see Section 4 and Table 1). The closed-loop systems were fed by the identical disturbance signals such as wind speed v_{w} and reactive power reference $q_{\mathrm{pcc,ref}}$. Since the reduced-order model (47) does not consider current dynamics, for this model no current controllers were implemented.

The comparative simulation results of all implementations are split into three plots:

- Figure 10 compares DC-link voltage u_{dc}, mechanical angular velocity ω_{m}, pitch angle β and tip speed ratio λ of all three models;
- Figure 11 compares turbine p_{t}, active p_{pcc} and reactive q_{pcc} power (at the PCC) and the produced energy E of all three models; and

- Figure 12 compares machine torque m_m of all three models and currents i_s^q, i_f^d, & i_f^q of full-order model and non-switching model.

Quantities of non-switching and reduced-order model are indicated by the additional subscript "nsm" and "rom", respectively. The quantities of the full-order model come without additional subscript.
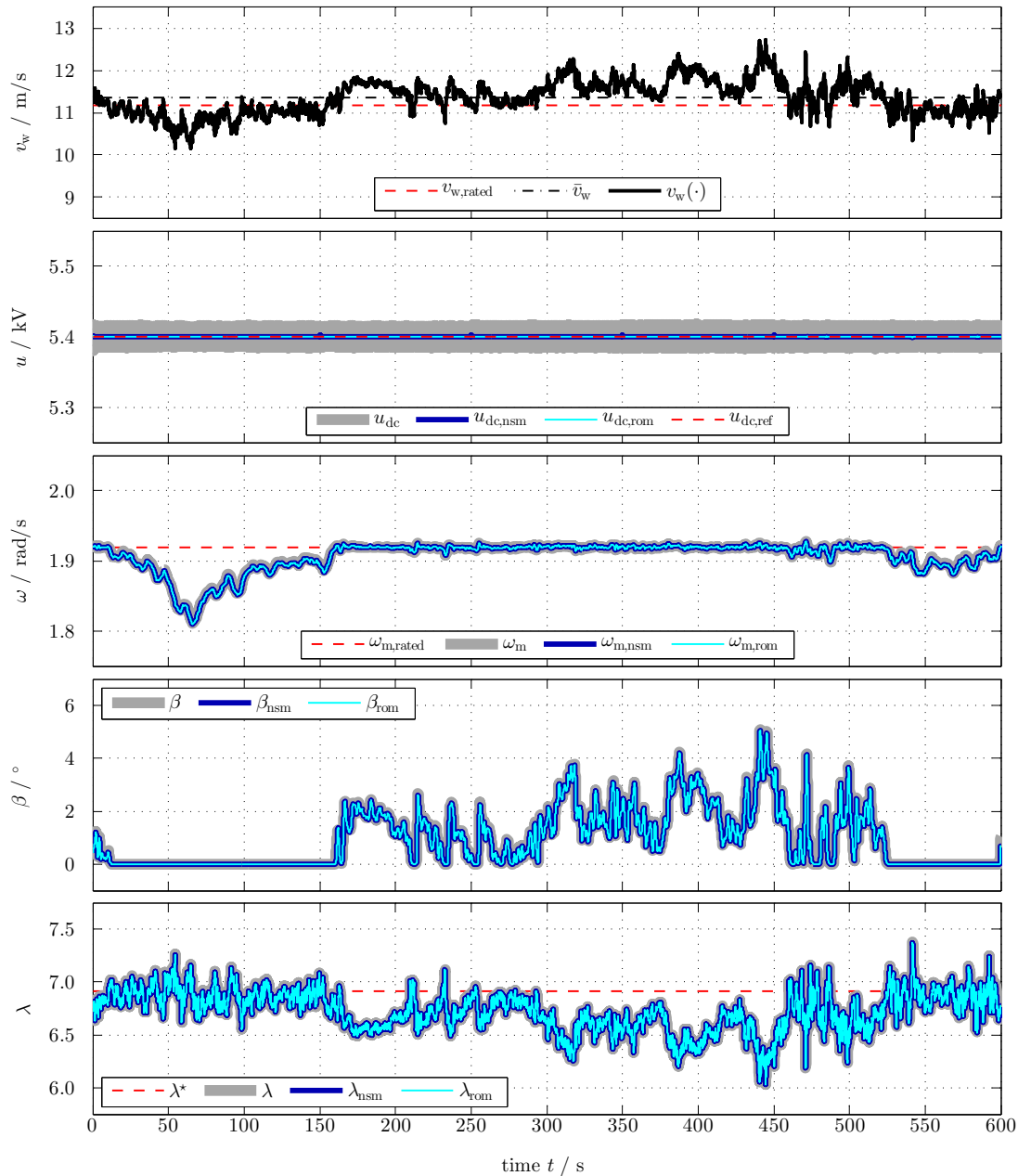

Figure 10. Comparison of DC-link voltages, mechanical angular velocities, and pitch angles.

The upper subplot in Figure 10 shows the wind speed v_w, its mean value $\bar{v}_\mathrm{w}$ and the nominal wind speed $v_\mathrm{w,rated}$ of the WTS. In the major part of the simulation (mainly around $t = 150, \ldots, 530\,\mathrm{s}$), the wind speed is significantly higher than the nominal wind speed of the turbine. Thus, the WTS models are operated in both considered regimes: regime II and regime III. The averaged wind speed is slightly above the nominal wind speed. In the second subplot, the DC-link voltages are depicted: $u_\mathrm{dc,nsm}$ (of non-switching model) and $u_\mathrm{dc,rom}$ (of reduced-order model) coincide and track their reference value of $5.4\,\mathrm{kV}$ nicely. The voltage u_dc (of the full-order model) also tracks its reference value but due to the modeled switching behavior of the power converters it is not as smooth as the other

DC-link voltages, where the switching is not considered in the models. Overall, all DC-link voltages, as DC sources of the power converters, can be considered as constant voltages. The third subplot shows the angular velocity of the shaft. The velocities of all three models are almost identical and do only exceed the nominal mechanical velocity $\omega_{\mathrm{m,rated}}$ for short periods. Hence, pitch and speed control system are working properly ensuring a correct operation of the WTS with (a) maximum power point tracking (MPPT) in regime II and (b) nominal power output (i.e., nominal speed and torque) in regime III. The pitch angles of all three implementations are shown in the fourth subplot. The three pitch controllers work—as expected—with very similar performance and are only active when the wind speed exceeds its nominal value (i.e., in regime III). In the last subplot, the tip speed ratios of the three implementations are shown; again, the three signal evolutions are almost identical. As long as pitching is deactivated, the turbine is operated in MPPT mode and the tip speed ratio is controlled to track the optimal tip speed ratio $\lambda^{\star}$. The control performance of the MPPT controller (34) is acceptable but rather slow (which is well known and could be accelerated by using inertia compensation techniques [52]).

　　　The first subplot of Figure 11 shows again the wind speed. The second subplot depicts nominal turbine power $p_{\mathrm{t,rated}}$, turbine power p_{t} and active power p_{pcc} at the PCC of all models. Within the time interval $[150\,\mathrm{s}, 530\,\mathrm{s})$, where the wind speed is (almost always) higher than the nominal wind speed of the turbine, the WTS is operated in regime III and nominal power is fed into the grid. Within the intervals $[0\,\mathrm{s}, 150\,\mathrm{s})$ and $[530\,\mathrm{s}, 600\,\mathrm{s}]$, the power output undergoes strong fluctuations. The WTS operates in regime II and follows the rapid variations of the wind power $p_{\mathrm{w}} \propto v_{\mathrm{w}}^3$ and the wind speed v_{w}. Maximum power point tracking is the control objective in regime II leading to varying speed (see third subplot in Figure 10) and machine torque (see third subplot in Figure 12). The principle behavior of all models is similar for both operating regimes. However, the switching behavior becomes only obvious in the active power of the full-order model. The active powers of the non-switching and reduced-order models represent the mean (averaged) output power of the full-order model. The reactive powers at the PCC are shown in the third subplot. The reference reactive power is followed almost instantaneously by all models (independently of being capacitive or inductive reactive power), which underpins the capability of WTSs to contribute to voltage stability of the power grid. The switching behavior in the reactive power is again only visible for the full-order model. The fourth subplot illustrates the produced energies of turbine $E_{\mathrm{t}} := \int p_{\mathrm{t}}\,\mathrm{d}t$ and induced energy $E_{\mathrm{pcc}} := \int p_{\mathrm{pcc}}\,\mathrm{d}t$ at the PCC (as integrals of powers over time). Due to the (copper) losses in generator and filter, the energy E_{t} produced by the turbine is slightly higher than the electrical energies of all three models induced at the PCC. The time evolutions of the electrical energies E_{pcc}, $E_{\mathrm{pcc,nsm}}$ and $E_{\mathrm{pcc,rom}}$ of the three models are (almost) not distinguishable. In conclusion, the induced energies E_{pcc}, $E_{\mathrm{pcc,nsm}}$ and $E_{\mathrm{pcc,rom}}$ at the PCC of all three models do match as well; which shows that the energy yield even of the simple third-order model is captured with sufficiently high accuracy.

　　　In the first subplot of Figure 12, again the wind speed is plotted. The second subplot shows the q-component of the stator current i_{s}^{q} for the full-order model and the non-switching model. The stator current i_{s}^{q} is proportional to the mechanical torque m_{m} and, thus, changes according to the respective wind speed v_{w} in regime II (maximum power point tracking with varying torque demand) and regime III (constant nominal torque). The reduced-order model does not consider the current dynamics. The non-switching model current represents the mean (average) current of the full-order model. In the third subplot, the generator torque is depicted. Its dynamics are similar to those of stator current or (negative) filter current (proportional to active power at the PCC). In regime III, the generator torque is almost constant at its nominal value (see interval $[150\,\mathrm{s}, 530\,\mathrm{s})$). The switching can only be observed in the torque of the full-order model, since it is proportional to the stator current which is directly affected by the switching in the converter. The torques of non-switching and reduced-order model can not be distinguished. The fourth and fifth subplots show the d- and q-components of the filter currents which are proportional to active power and reactive power at the PCC, respectively. In both subplots, the non-switching model gives again the averaged currents of the full-order model. As the currents dynamics of the reduced-order model are not simulated, these currents are not shown.
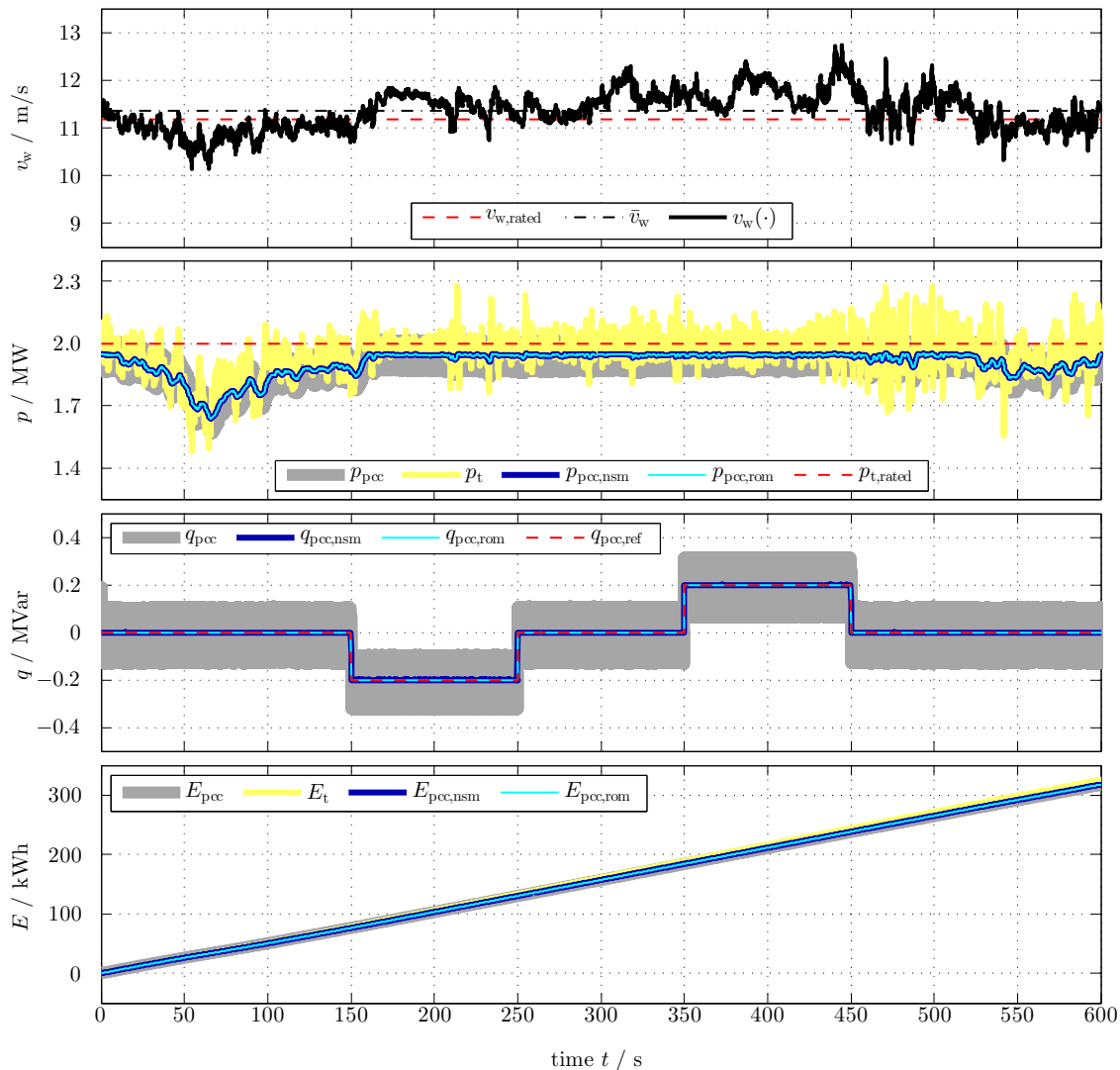
Figure 11. Comparison of active and reactive powers, and produced energy.

Table 2 compares the implementation environments and the duration of the simulations of all three implementations. All simulations were performed on the same Intel Xenon computer having Windows 10 (Education 64-bit) as operating system. All three models were implemented in Matlab/Simulink R2013b (64-bit). The three simulations were run with the same fixed-step solver Runge-Kutta (ode4) but differing step sizes (to capture the switching effects considered in the full-order model). To compute active and reactive power over the scenario duration of 00:10 h = 600 s (see e.g., Figure 10), the simulation time of the full-order model is (a) almost 670 times longer (with 2:58 h) than that of the non-switching model (with 16 s) and (b) more than 970 times longer than that of the reduced-order model (with 11 s). This is due to the higher complexity of the full-order model and due to the smaller simulation step size (4×10^{-6} s) required to simulate the switching behavior of the converters correctly. Neglecting the switching behavior allows the use of larger simulation step sizes (2×10^{-3} s). So, the simulation durations of the non-switching and reduced-order model are, both, much shorter than 1 min. The simulations of the non-switching and reduced-order model (not considering the switching of the power electronics) could even be further accelerated by using variable-step solvers.
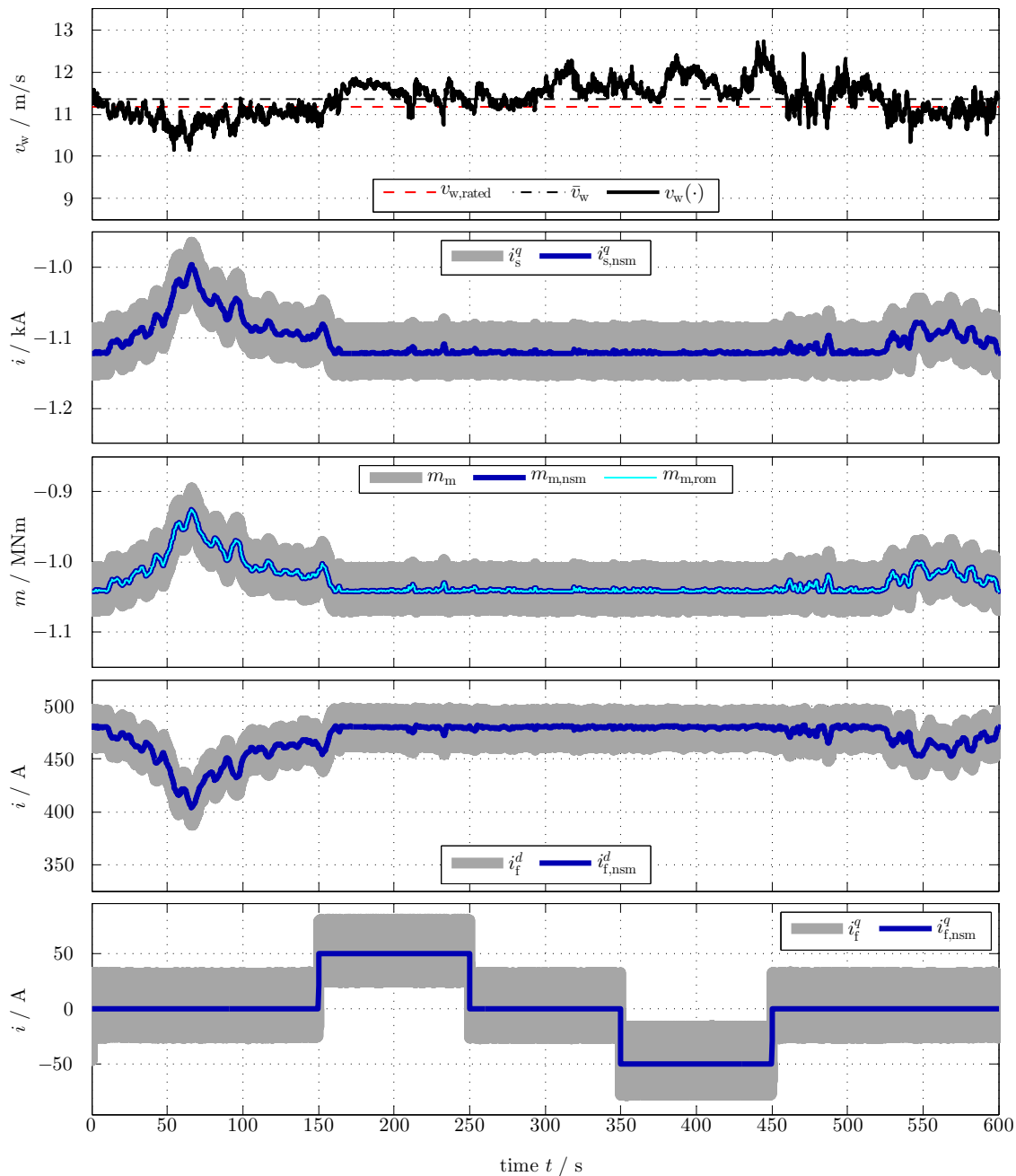
Figure 12. Comparison of torques, and machine-side and filter-side currents (if available in model).

Remark 4. *The simulations were also implemented on a less powerful Windows 10 (Home 64-bit) standard PC with four Intel Core i7-3630QM CPUs (2.40 GHz) and 8000 MB RAM. The closed-loop systems of the non-switching and the reduced-order models were simulated using Matlab/Simulink (R2016a 64-bit) and OpenModelica (v1.11.0 64-bit) with the identical solver as in Table 1 but reduced step size (2×10^{-4} s). Although the computational power of the Intel Xenon computer is significantly higher than that of the standard PC (three times more cores with higher frequency; memory 15 times larger), the simulation durations of the non-switching and reduced-order model on the standard PC were also quite fast and lower than three minutes with 170 s and 119 s, respectively. Moreover, the ratios of these two simulation durations are very similar with $11/16 = 0.6875 \approx 119/170 = 0.7$, which shows that the non-switching and reduced-order models are well suited for "real-time" simulation even on standard PCs.*

Table 2. Simulation environments and durations.

	Full-Order Model (29)	Non-Switching Model (40)	Reduced-Order Model (47)
order	9	7	3
OS	Windows 10 (Education 64-bit)	Windows 10 (Education 64-bit)	Windows 10 (Education 64-bit)
CPU	Intel Xenon E5-1650 v3 (3.50 GHz, 12 CPUs)	Intel Xenon E5-1650 v3 (3.50 GHz, 12 CPUs)	Intel Xenon E5-1650 v3 (3.50 GHz, 12 CPUs)
RAM	131,072 MB	131,072 MB	131,072 MB
Software	Matlab Simulink (R2013b 64-bit)	Matlab Simulink (R2016a 64-bit)	Matlab Simulink (R2016a 64-bit)
Step size	$4 \times 10^{-6}\,\text{s}$	$2 \times 10^{-3}\,\text{s}$	$2 \times 10^{-3}\,\text{s}$
Solver	Runge-Kutta (ode4)	Runge-Kutta (ode4)	Runge-Kutta (ode4)
Duration	10,680 s (2:58 h)	16 s	11 s

7. Conclusions

Existing control-oriented models of wind turbine systems (WTS) are subject to rather poorly motivated simplifications. In this paper, physically motivated full-order and reduced-order state-space models for variable-speed variable-pitch WTSs with permanent magnet synchronous generator (PMSG) are presented. Initially, the system under consideration and the relevant wind speed operating regions are described. Afterwards, an 11th-order state-space model in the three-phase (a, b, c)-reference frame is presented. The derived full-order model considers all relevant effects (including the switching behavior of the power converters) which significantly affect the active and reactive power output of the system. By transforming the 11th-order model to its equivalent representation in the synchronously rotating (d, q)-reference frame, a 9th-order state-space model is obtained. A complete control and operation management scheme for the WTS is proposed. The control schemes cover practical constraints such as saturation and integral windup effects, and enable implementation and analysis of the complete closed-loop WTS model. Based on the 9th-order model, by invoking a structured and physically motivated model reduction procedure, a non-switching 7th-order model and a simple 3rd-order model are finally derived. The reduced-order models still capture dominant system dynamics and losses of the considered WTS. Moreover, the reduced-order state-space models come with a significant reduction of computation/simulation time and controller design complexity. The validity of the reduced-order models against their underlying full-order model is shown by numerical simulations using the introduced control and operation management schemes and a realistic wind speed profile (covering regimes II + III). It is shown that full-order and reduced-order models produce plausible and (very) comparable results. Due to the modeled switching in the power converters, the full-order models exhibit realistic high frequency oscillations in the instantaneous power output. In contrast, the non-switching 7th-order and 3rd-order models can only provide a time-averaged instantaneous power output. Nevertheless, both reduced-order models correctly reflect the (average) energy production of the considered WTS. Regarding the power output, the simulations suggest no significant difference between the non-switching 7th-order model and the 3rd-order model. Thus, for dynamical power flow-based studies or controller design in large-scale power systems, the proposed and validated 3rd-order model produces sufficiently exact (simulation) results and allows for a reasonably fast computation.

Nomenclature

Mathematical symbols and functions

$\mathbb{N}, \mathbb{R}, \mathbb{C}$	natural, real, complex numbers
$\mathbb{R}_{>\alpha} := (\alpha, \infty);$ $(\mathbb{R}_{\geq\alpha} := [\alpha, \infty))$	real numbers greater than (and equal to) $\alpha \in \mathbb{R}$
$\mathcal{C}(I; Y)$	space of continuous functions mapping $I \to Y$
$\boldsymbol{x} := (x_1, \ldots, x_n)^\top \in \mathbb{R}^n$	column vector with $n \in \mathbb{N}$ (where "$\top$" and ":=" mean "transposed" and "is defined as", resp.)
$\boldsymbol{0}_n \in \mathbb{R}^n; \boldsymbol{1}_n \in \mathbb{R}^n$	zero; unity vector
$\boldsymbol{a}^\top \boldsymbol{b} := a_1 b_1 + \cdots + a_n b_n$	scalar product of the vectors $\boldsymbol{a} := (a_1, \ldots, a_n)^\top$ and $\boldsymbol{b} := (b_1, \ldots, b_n)^\top$
$\boldsymbol{A} \in \mathbb{R}^{n \times n}$	(square) matrix with n rows and columns
$\boldsymbol{A}^{-1}; \boldsymbol{A}^{-\top} \in \mathbb{R}^{n \times n}$	inverse matrix; transposed inverse of $\boldsymbol{A}$ (if exists).
$\boldsymbol{I}_n \in \mathbb{R}^{n \times n}; \boldsymbol{O}_{n \times p} \in \mathbb{R}^{n \times p}$	identity; zero matrix with $p \in \mathbb{N}$
$\mathrm{sat}_a^b(x) \colon \mathbb{R} \to [a, b]$ $\mathbf{sat}_{\widehat{u}}(\boldsymbol{x}) \colon$ $\mathbb{R}^n \to \{\boldsymbol{x} \in \mathbb{R}^n \,\vert\, \|\boldsymbol{x}\| \leq \widehat{u}\}$	saturation functions, for $b > a$ and $\widehat{u} > 0$, given by

$$\mathrm{sat}_a^b(x) := \begin{cases} b & , x \geq b \\ x & , a < x < b \; ; \\ a & , x \leq a. \end{cases} \qquad \mathbf{sat}_{\widehat{u}}(\boldsymbol{x}) := \begin{cases} \widehat{u}\dfrac{\boldsymbol{x}}{\|\boldsymbol{x}\|} & , \|\boldsymbol{x}\| \geq \widehat{u} \\ \boldsymbol{x} & , \|\boldsymbol{x}\| < \widehat{u}. \end{cases} \tag{48}$$

$f_{\hat{a}, \Delta} \colon \mathbb{R} \to [0, 1]$	transition function, for $\hat{a} \in \mathbb{R}$ and $\Delta > 0$, given by

$$f_{\hat{a}, \Delta}(x) := \begin{cases} 0 & , x \geq \hat{a} \\ \dfrac{-x + \hat{a}}{\Delta} & , \hat{a} - \Delta \leq x < \hat{a} \; . \\ 1 & , x < \hat{a} - \Delta \end{cases} \tag{49}$$

Reference frames and transformation/rotation matrices for modeling

$\boldsymbol{x}^{abc} := \left(x^a, x^b, x^c\right)^\top \in \mathbb{R}^3$ 　　quantity vector in the three-phase (a, b, c)-reference frame

$\boldsymbol{x}^{dq} = \left(x^d, x^q\right)^\top \in \mathbb{R}^2$ 　　quantity vector in the synchronously rotating (d, q)-reference frame

$\boldsymbol{T}_{\mathrm{cp}}(\phi_\mathrm{p}) \in \mathbb{R}^{2\times3};$
$\boldsymbol{T}_{\mathrm{cp}}(\phi_\mathrm{p})^{-1} \in \mathbb{R}^{3\times2}$ 　　(reduced) Clarke-Park-transformation matrix; its inverse matrix, relating $\boldsymbol{x}^{dq} = \boldsymbol{T}_{\mathrm{cp}}(\phi_\mathrm{p})\boldsymbol{x}^{abc}$, and, for $\kappa \in \left\{\frac{2}{3}, \sqrt{\frac{2}{3}}\right\}$ given by [60] (Appendix A.5)

$$\boldsymbol{T}_{\mathrm{cp}}(\phi_\mathrm{p}) := \kappa \begin{bmatrix} \cos(\phi_\mathrm{p}) & \cos\left(\phi_\mathrm{p} - \frac{2\pi}{3}\right) & \cos\left(\phi_\mathrm{p} - \frac{4\pi}{3}\right) \\ -\sin(\phi_\mathrm{p}) & -\sin\left(\phi_\mathrm{p} - \frac{2\pi}{3}\right) & -\sin\left(\phi_\mathrm{p} - \frac{4\pi}{3}\right) \end{bmatrix} \text{ and } \boldsymbol{T}_{\mathrm{cp}}(\phi_\mathrm{p})^{-1} := \frac{2}{3\kappa} \begin{bmatrix} \cos(\phi_\mathrm{p}) & -\sin(\phi_\mathrm{p}) \\ \cos\left(\phi_\mathrm{p} - \frac{2\pi}{3}\right) & -\sin\left(\phi_\mathrm{p} - \frac{2\pi}{3}\right) \\ \cos\left(\phi_\mathrm{p} - \frac{4\pi}{3}\right) & -\sin\left(\phi_\mathrm{p} - \frac{4\pi}{3}\right) \end{bmatrix}. \tag{50}$$

$\boldsymbol{J} \in \mathbb{R}^{2\times2}; \boldsymbol{J}_\Sigma \in \mathbb{R}^{3\times3}$ 　　rotation matrices (counter-clock wise by $\frac{\pi}{2}$), given by

$$\boldsymbol{J} := \begin{bmatrix} 0 & -1 \\ 1 & 0 \end{bmatrix} \quad \text{and} \quad \boldsymbol{J}_\Sigma := \frac{1}{\sqrt{3}} \begin{bmatrix} 0 & -1 & 1 \\ 1 & 0 & -1 \\ -1 & 1 & 0 \end{bmatrix}. \tag{51}$$

Physical quantitities

$\boldsymbol{u}_\mathrm{s}^{abc}; \boldsymbol{i}_\mathrm{s}^{abc}; \boldsymbol{u}_\mathrm{s}^{dq}\, \boldsymbol{i}_\mathrm{s}^{dq}; p_\mathrm{s}$ 　　*stator* voltages; currents in (a, b, c) or (d, q)-reference frame; power

$R_\mathrm{s}; L_\mathrm{s}; L_\mathrm{s,m}; L_{\mathrm{s},\sigma}$ 　　*stator* resistance; main; mutual; leakage (stray) inductance

$\boldsymbol{L}_\mathrm{s}^{abc}; \boldsymbol{L}_\mathrm{s}^{dq}$ 　　*stator* inductance matrices in (a, b, c) or (d, q)-reference frame

$\boldsymbol{\psi}_\mathrm{s}^{abc}; \boldsymbol{\psi}_\mathrm{s}^{dq}; \boldsymbol{\psi}_\mathrm{pm}^{abc}; \boldsymbol{\psi}_\mathrm{pm}^{dq}$ 　　*stator* and *permanent-magnet* flux linkages in (a, b, c) or (d, q)-reference frame

$\boldsymbol{u}_\mathrm{f}^{abc}; \boldsymbol{i}_\mathrm{f}^{abc}; \boldsymbol{u}_\mathrm{f}^{dq}; \boldsymbol{i}_\mathrm{f}^{dq}; p_\mathrm{f}$ 　　*filter* voltages; currents in (a, b, c) or (d, q)-reference frame; power

$R_\mathrm{f}; L_\mathrm{f}$ 　　*filter* resistance; inductance

$\boldsymbol{u}_\mathrm{g}^{abc}; \boldsymbol{u}_\mathrm{g}^{dq}; \hat{u}_\mathrm{g}; \phi_\mathrm{g}; \omega_\mathrm{g}$ 　　*grid* voltages in (a, b, c) or (d, q)-reference frame; voltage amplitude; angle; angular frequency

$u_\mathrm{dc}; i_\mathrm{dc}; p_\mathrm{dc}; C_\mathrm{dc}$ 　　*DC-link* voltage; current; power; capacitance

$\boldsymbol{s}_\mathrm{s}^{abc}; \boldsymbol{s}_\mathrm{f}^{abc}; f_\mathrm{sw}$ 　　*switching* vector for machine (stator); grid (filter); switching frequency

$\omega_\mathrm{t}; m_\mathrm{t}; r_\mathrm{t}; p_\mathrm{t}; \Theta_\mathrm{t}; g_\mathrm{r}$ 　　*turbine* angular frequency; torque; radius; power; inertia; gear ratio

$v_\mathrm{w}; p_\mathrm{w}; \beta; \lambda := \frac{r_\mathrm{t}\omega_\mathrm{t}}{v_\mathrm{w}}; c_\mathrm{p}$ 　　*wind* speed; power; pitch angle; tip speed ratio; power coefficient

$\phi_\mathrm{m}; \omega_\mathrm{m}; m_\mathrm{m}; p_\mathrm{m}; \Theta_\mathrm{m}; n_\mathrm{p}$ 　　*machine* (generator) angular position; angular frequency; torque; power; inertia; number of pole pairs

$p_\mathrm{pcc}; q_\mathrm{pcc}$ 　　active; reactive (instantaneous) power at point of common coupling (PCC)

References

1. Global Wind Energy Council. *Global Wind Report 2017*; Technical Report; GWEC: Brussels, Belgium, 2017.
2. Park, G.L. Planning Manual for Utility Application of WECS. In *Technical Report, Michigan State University, East Lansing (USA)*; Division of Engineering Research: Room, Italy, 1979.
3. Øye, S. Unsteady Wake Effects Caused by Pitch-Angle Changes. In *IEA R&D WECS Joint Action on Aerodynamics of Wind Turbines*; IEA: Paris, France, 1986; pp. 58–79.
4. Anderson, P.M.; Bose, A. Stability Simulation of Wind Turbine Systems. *IEEE Trans. Power Appar. Syst.* **1983**, *PAS-102*, 3791–3795.
5. Petru, T.; Thiringer, T. Modeling of Wind Turbines for Power System Studies. *IEEE Trans. Power Syst.* **2002**, *17*, 1132–1139. [CrossRef]
6. Papathanassiou, S.A.; Papadopoulos, M.P. Dynamic Behavior of Variable Speed Wind Turbines under Stochastic Wind. *IEEE Trans. Energy Convers.* **1999**, *14*, 1617–1623. [CrossRef]
7. Wu, B.; Lang, Y.; Zargari, N.; Kouro, S. *Power Conversion and Control of Wind Energy Systems*; John Wiley & Sons: Hoboken, NJ, USA, 2011.
8. Behnke, M.; Ellis, A.; Kazachkov, Y.; McCoy, T.; Muljadi, E.; Price, W.; Sanchez-Gasca, J. *Development and Validation of WECC Variable Speed Wind Turbine Dynamic Models for Grid Integration Studies*; Technical Report, National Renewable Energy Laboratory (NREL); U.S. Department of Energy: Washington, DC, USA, 2007.
9. Kojabadi, H.M.; Chang, L.; Boutot, T. Development of a Novel Wind Turbine Simulator for Wind Energy Conversion Systems Using an Inverter-Controlled Induction Motor. *IEEE Trans. Energy Convers.* **2004**, *19*, 547–552. [CrossRef]
10. Slootweg, J.G.; Polinder, H.; Kling, W.L. Dynamic Modelling of a Wind Turbine with Doubly Fed Induction Generator. In Proceedings of the Power Engineering Society Summer Meeting, Vancouver, BC, Canada, 15–19 July 2001; pp. 644–649.
11. Miller, N.W.; Sanchez-Gasca, J.J.; Price, W.W.; Delmerico, R.W. Dynamic Modeling of GE 1.5 and 3.6 MW Wind Turbine-Generators for Stability Simulations. In Proceedings of the IEEE Power Engineering Society General Meeting, Toronto, ON, Canada, 13–17 July 2003; pp. 1977–1983.
12. Ekanayake, J.B.; Holdsworth, L.; Wu, X.; Jenkins, N. Dynamic Modeling of Doubly Fed Induction Generator Wind Turbines. *IEEE Trans. Power Syst.* **2003**, *18*, 803–809. [CrossRef]
13. Lei, Y.; Mullane, A.; Lightbody, G.; Yacamini, R. Modeling of the Wind Turbine with a Doubly Fed Induction Generator for Grid Integration Studies. *IEEE Trans. Energy Convers.* **2006**, *21*, 257–264. [CrossRef]
14. Chowdhury, B.H.; Chellapilla, S. Double-Fed Induction Generator Control for Variable Speed Wind Power Generation. *Electr. Power Syst. Res.* **2006**, *76*, 786–800. [CrossRef]
15. Sun, Z.; Wang, H.; Li, Y. Modelling and Simulation of Doubly-Fed Induction Wind Power System Based on Matlab/Simulink. In Proceedings of the International Conference on Sustainable Power Generation and Supply, Hangzhou, China, 8–9 September 2012.
16. Subramanian, C.; Casadei, D.; Tani, A.; Rossi, C. Modeling and Simulation of Grid Connected Wind Energy Conversion System Based on a Doubly Fed Induction Generator (DFIG). *Int. J. Electr. Energy* **2014**, *2*. [CrossRef]
17. Singh, M.; Santoso, S. *Dynamic Models for Wind Turbines and Wind Power Plants*; Technical Report, National Renewable Energy Laboratory (NREL); U.S. Department of Energy: Washington, DC, USA, 2011.
18. Lalor, G.; Mullane, A.; O'Malley, M. Frequency control and wind turbine technologies. *IEEE Trans. Power Syst.* **2005**, *20*, 1905–1913. [CrossRef]
19. Tobías-González, A.; Pena-Gallardo, R.; Morales-Saldana, J.; Gutiérrez-Urueta, G. Modeling of a Wind Turbine with a Permanent Magnet Synchronous Generator for Real Time Simulations. In Proceedings of the 2015 IEEE International Autumn Meeting on Power, Electronics and Computing, Ixtapa, Mexico, 4–6 November 2015; pp. 1–6.
20. Singh, M.; Santoso, S. Dynamic Model for Full-Converter Wind Turbines Employing Permanent Magnet Alternators. In Proceedings of the IEEE Power and Energy Society General Meeting, Detroit, MI, USA, 24–29 July 2011.
21. Yin, M.; Li, G.; Zhou, M.; Zhao, C. Modeling of the Wind Turbine with a Permanent Magnet Synchronous Generator for Integration. In Proceedings of the Power Engineering Society General Meeting, Tampa, FL, USA, 24–28 June 2007; pp. 1–6.

22. Sanchez, J.A.; Veganzones, C.; Martinez, S.; Blazquez, F.; Herrero, N.; Wilhelmi, J.R. Dynamic Model of Wind Energy Conversion Systems with Variable Speed Synchronous Generator and Full-Size Power Converter for Large-Scale Power System Stability Studies. *Renew. Energy* **2008**, *33*, 1186–1198. [CrossRef]

23. Rolan, A.; Luna, A.; Vazquez, G.; Aguilar, D.; Azevedo, G. Modeling of a Variable Speed Wind Turbine With a Permanent Magnet Synchronous Generator. In Proceedings of the IEEE International Symposium on Industrial Electronics, Seoul, South Korea, 5–8 July 2009; pp. 734–739.

24. Elbeji, O.; Hamed, M.B.; Sbita, L. PMSG Wind Energy Conversion System: Modeling and Control. *Int. J. Mod. Nonlinear Theory Appl.* **2014**, *3*, 88–97. [CrossRef]

25. Rekioua, D. Wind Energy Conversion and Power Electronics Modeling. In *Wind Power Electric System: Modeling, Simulation and Control*; Springer: Berlin, Germany, 2014; pp. 51–76.

26. Munteanu, I.; Bratcu, A.I.; Cutululis, N.A.; Ceanga, E. *Optimal Control of Wind Energy Systems*; Springer: Berlin, Germany, 2008.

27. Burton, T.; Sharpe, D.; Jenkins, N.; Bossanyi, E. *Wind Energy Handbook*; John Wiley & Sons: Hoboken, NJ, USA, 2001.

28. Schlipf, D.; Schlipf, D.; Kühn, M. Nonlinear model predictive control of wind turbines using LIDAR. *Wind Energy* **2012**, *16*, 1107–1129. [CrossRef]

29. Zribi, M.; Alrifai, M.; Rayan, M. Sliding Mode Control of a Variable-Speed Wind Energy Conversion System Using a Squirrel Cage Induction Generator. *Energies* **2017**, *10*, 604. [CrossRef]

30. Soliman, M.; Malik, O.P.; Westwick, D.T. Multiple Model Predictive Control for Wind Turbines with Doubly Fed Induction Generators. *IEEE Trans. Sustain. Energy* **2011**, *2*, 215–225. [CrossRef]

31. Bououden, S.; Chadli, M.; Filali, S.; El Hajjaji, A. Fuzzy Model Based Multivariable Predictive Control of a Variable Speed Wind Turbine: LMI Approach. *Renew. Energy* **2012**, *37*, 434–439. [CrossRef]

32. Rocha, R.; Martins Filho, L.S.M.; Bortolus, M.V. Optimal Multivariable Control for Wind Energy Conversion System—A Comparison Between H_2 and H_∞ Controllers. In Proceedings of the Conference on Decision and Control and the European Control Conference, Seville, Spain, 15 December 2005; pp. 7906–7911.

33. Henriksen, L.C.; Poulsen, N.K.; Hansen, M.H. Nonlinear Model Predictive Control of a Simplified Wind Turbine. In *IFAC World Congress*; Elsevier: New York, NY, USA, 2011; pp. 551–556.

34. Liu, X.; Kong, X. Nonlinear Model Predictive Control for DFIG-Based Wind Power Generation. *IEEE Trans. Autom. Sci. Eng.* **2014**, *11*, 1046–1055. [CrossRef]

35. Yaramasu, V.; Wu, B.; Rivera, M.; Rodriguez, J. A New Power Conversion System for Megawatt PMSG Wind Turbines Using Four-Level Converters and a Simple Control Scheme Based on Two-Step Model Predictive Strategy—Part I: Modeling and Theoretical Analysis. *IEEE J. Emerg. Sel. Top. Power Electron.* **2014**, *2*, 3–13. [CrossRef]

36. Lin, W.M.; Hong, C.M.; Ou, T.C.; Chiu, T.M. Hybrid intelligent control of PMSG wind generation system using pitch angle control with RBFN. *Energy Convers. Manag.* **2011**, *52*, 1244–1251. [CrossRef]

37. Ou, T.C.; Lu, K.H.; Huang, C.J. Improvement of Transient Stability in a Hybrid Power Multi-System Using a Designed NIDC (Novel Intelligent Damping Controller). *Energies* **2017**, *10*, 488. [CrossRef]

38. Zhang, Z.; Li, Z.; GAE, M.P.K.; Rodriguez, J.; GAE, R.K. Robust Predictive Control of Three-Level NPC Back-to-Back Converter PMSG Wind Turbine Systems with Revised Predictions. *IEEE Trans. Power Electron.* **2018**, 1. [CrossRef]

39. Arani, M.F.M.; Mohamed, Y.A.R.I. Assessment and Enhancement of a Full-Scale PMSG-Based Wind Power Generator Performance Under Faults. *IEEE Trans. Energy Convers.* **2016**, *31*, 728–739. [CrossRef]

40. Shahriari, S.A.A.; Raoofat, M.; Dehghani, M.; Mohammadi, M.; Saad, M. Dynamic state estimation of a permanent magnet synchronous generator-based wind turbine. *IET Renew. Power Gener.* **2016**, *10*, 1278–1286. [CrossRef]

41. Yu, S.; Emami, K.; Fernando, T.; Iu, H.H.C.; Wong, K.P. State estimation of doubly fed induction generator wind turbine in complex power systems. *IEEE Trans. Power Syst.* **2016**, *31*, 4935–4944. [CrossRef]

42. Huerta, F.; Tello, R.L.; Prodanovic, M. Real-Time Power-Hardware-in-the-Loop Implementation of Variable-Speed Wind Turbines. *IEEE Trans. Ind. Electron.* **2017**, *64*, 1893–1904. [CrossRef]

43. Bianchi, F.D.; Mantz, R.J.; De Battista, H. Modelling of Variable-Speed Variable-Pitch Wind Energy Conversion Systems. In *Wind Turbine Control Systems: Principles, Modelling and Gain Scheduling Design*; Springer: Berlin, Germany, 2007; pp. 29–48.

44. Schubert, M. Verfahren Zur Regelung Einer Windenergieanlage und Windenergieanlage mit Einem Rotor. Germany Patent DE102004054608B4, 29 June 2006.

45. Dirscherl, C.; Hackl, C.; Schechner, K. Modellierung und Regelung von modernen Windkraftanlagen: Eine Einführung (see https://arxiv.org/abs/1703.08661 for the English translation). In *Elektrische Antriebe—Regelung von Antriebssystemen*; Schröder, D., Ed.; Springer: Berlin, Germany, 2015; Chapter 24, pp. 1540–1614.

46. Betz, A. *Wind-Energie und ihre Ausnutzung durch Windmühlen*; Vandenhoeck & Ruprecht: Göttingen, Germany, 1926.

47. Heier, S. *Windkraftanlagen: Systemauslegung, Netzintegration und Regelung*, 5th ed.; Springer Vieweg+Teubner Verlag: Berlin, Germany, 2009.

48. Hackl, C.M. *Non-identifier based adaptive control in mechatronics: Theory and Application*; Number 466 in Lecture Notes in Control and Information Sciences; Springer International Publishing: Berlin, Germany, 2017. doi:10.1007/978-3-319-55036-7.

49. Koch, F.W. Simulation und Analyse der Dynamischen Wechselwirkung von Windenergieanlagen mit dem Elektroenergiesystem. Ph.D. Thesis, Universität Duisburg-Essen, Duisburg, Germany, 2005.

50. Slootweg, J.; De Haan, S.W.H.; Polinder, H.; Kling, W. General model for representing variable speed wind turbines in power system dynamics simulations. *IEEE Trans. Power Syst.* **2003**, *18*, 144–151. [CrossRef]

51. Slootweg, J.G.; Polinder, H.; Kling, W.L. Initialization of wind turbine models in power system dynamics simulations. In Proceedings of the 2001 IEEE Porto Power Tech Proceedings (Cat. No.01EX502), Porto, Portugal, 10–13 September 2001; Volume 4, p. 6. [CrossRef]

52. Eldeeb, H.; Hackl, C.M.; Kullick, J. Efficient operation of anisotropic synchronous machines for wind energy systems. In Proceedings of the 6th Edition of the Conference "The Science of Making Torque from Wind" (TORQUE 2016), Munich, Germany, 5–7 October 2016; Volume 753, doi:10.1088/1742-6596/753/11/112009.

53. Blaabjerg, F.; Liserre, M.; Ma, K. Power Electronics Converters for Wind Turbine Systems. *IEEE Trans. Ind. Appl.* **2012**, *48*, 708–718. [CrossRef]

54. Schröder, D. *Leistungselektronische Schaltungen: Funktion, Auslegung und Anwendung*; Springer: Berlin, Germany, 2012.

55. Bernet, S. *Selbstgeführte Stromrichter am Gleichspannungszwischenkreis: Funktion, Modulation und Regelung*; Springer: Berlin, Germany, 2012.

56. Holmes, D.G.; Lipo, T.A. *Pulse Width Modulation For Power Converters*; IEEE Series on Power Engineering; IEEE Press: Piscataway, NJ, USA, 2003.

57. Schröder, D. *Leistungselektronische Schaltungen—Funktion, Auslegung und Anwendung (2. Auflage)*; Springer: Berlin, Germany, 2008.

58. Böcker, J.; Beineke, S.; Bähr, A. On the Control Bandwidth of Servo Drives. In Proceedings of the 13th European Conference on Power Electronics and Applications, Barcelona, Spain, 8–10 September 2009; pp. 1–10.

59. DIN Deutsches Institut für Normung e. V. *DIN EN 50160:2011-02: Merkmale der Spannung in öffentlichen Elektrizitätsversorgungsnetzen*; Norm 2011-02; Beuth Verlag: Berlin, Germany, 2011.

60. Teodorescu, R.; Liserre, M.; Rodriguez, P. *Grid Converters for Photovoltaic and Wind Power Systems*; John Wiley & Sons, Ltd.: Chichester, UK, 2011.

61. Dirscherl, C.; Fessler, J.; Hackl, C.M.; Ipach, H. State-feedback controller and observer design for grid-connected voltage source power converters with LCL-filter. In Proceedings of the 2015 IEEE International Conference on Control Applications (CCA), Sydney, NSW, Australia, 21–23 September 2015; pp. 215–222. [CrossRef]

62. Hackl, C.M. MPC with analytical solution and integral error feedback for LTI MIMO systems and its application to current control of grid-connected power converters with LCL-filter. In Proceedings of the 2015 IEEE International Symposium on Predictive Control of Electrical Drives and Power Electronics (PRECEDE), Valparaiso, Chile, 5–6 October 2015; pp. 61–66. [CrossRef]

63. Schröder, D. *Elektrische Antriebe—Regelung von Antriebssystemen (3., Bearb. Auflage)*; Springer: Berlin, Germany, 2009.

64. Hackl, C.M. On the equivalence of proportional-integral and proportional-resonant controllers with anti-windup. *arXiv* **2016**, arXiv:1610.07133.

65. Åström, K.J.; Rundqwist, L. Integrator windup and how to avoid it. In Proceedings of the American Control Conference, Pittsburgh, PA, USA, 21–23 June 1989; pp. 1693–1698.

66. Peng, Y.; Vranic, D.; Hanus, R. Anti-windup, bumpless, and conditioned transfer techniques for PID controllers. *IEEE Control Syst. Mag.* **1996**, *16*, 48–57. [CrossRef]

67. Kessler, G. Über die Vorausberechnung optimal abgestimmter Regelkreise—Teil 3: Die optimale Einstellung des Reglers nach dem Betragsoptimum. *Regelungstechnik* **1955**, *3*, 40–49.

68. Hackl, C.; Schechner, K. Non-ideal feedforward torque control of wind turbines: Impacts on annual energy production & gross earnings. *J. Phys.* **2016**, *753*, 112010.

69. Mullen, J.; Hoagg, J.B. Wind Turbine Torque Control for Unsteady Wind Speeds Using Approximate-Angular-Acceleration Feedback. In Proceedings of the 52nd IEEE Conference on Decision and Control (CDC), Florence, Italy, 10–13 December 2013; pp. 397–402.

70. Dirscherl, C.; Hackl, C.M.; Schechner, K. Pole-placement based nonlinear state-feedback control of the DC-link voltage in grid-connected voltage source power converters: A preliminary study. In Proceedings of the 2015 IEEE International Conference on Control Applications (CCA) (CCA), Sydney, NSW, Australia, 21–23 September 2015; pp. 207–214. [CrossRef]

71. Schechner, K.; Bauer, F.; Hackl, C.M. Nonlinear DC-link PI control for airborne wind energy systems during pumping mode. In *Airborne Wind Energy: Advances in Technology Development and Research*; Schmehl, R., Ed.; Springer: Berlin, Germany, 2016.

72. Lescher, F.; Zhao, J.Y.; Borne, P. Switching LPV Controllers for a Variable Speed Pitch Regulated Wind Turbine. In Proceedings of the IMACS Multiconference on Computational Engineering in Systems Applications, Beijing, China, 4–6 October 2006; pp. 1334–1340.

73. Duindam, V.; Macchelli, A.; Stramigioli, S.; Bruyninckx, H., Eds. *Modeling and Control of Complex Physical Systems: The Port-Hamiltonian Approach*; Springer: Berlin/Heidelberg, Germany, 2009.